**Preprint**

Guo, L., Latham, J.-P., and Xiang, J. (2015). Numerical simulation of breakages of concrete armour units using a three-dimensional fracture model in the context of the combined finite-discrete element method. *Computers & Structures*, 146:117-142.

http://dx.doi.org/10.1016/j.compstruc.2014.09.001

# Numerical simulation of breakages of concrete armour units using a three-dimensional fracture model in the context of the combined finite-discrete element method

Liwei Guo*, John-Paul Latham and Jiansheng Xiang

*Department of Earth Science and Engineering, Imperial College London, South Kensington Campus, London SW7 2AZ, United Kingdom*

*E-mail address*: liwei.guo@ucl.ac.uk (Liwei Guo), j.p.latham@imperial.ac.uk (John-Paul Latham), j.xiang@imperial.ac.uk (Jiansheng Xiang).

## Abstract

Rubble-mound breakwaters covered by armour layers of concrete units are widely used coastal structures. In this work, a three-dimensional fracture model in the context of the combined finite-discrete element method is applied to investigate the structural integrity of two types of concrete armour units under dynamic and extreme loading conditions. Dolosse units are simulated in drop tests and pendulum tests, and Core-Loc units of prototype scale

---

* Corresponding author. Tel.: +44 20 3108 9514.
E-mail address: liwei.guo@ucl.ac.uk (Liwei Guo).
Present address: Department of Mechanical Engineering, University College London, Torrington Place, London WC1E 7JE, United Kingdom.

Abbreviation in this paper:
FEMDEM: combined finite-discrete element method.

are simulated under an imaginary extreme loading condition. The whole structural response of concrete armour units is accurately captured and the results provide a better understanding of damage and reserve stability of such systems.

***Keywords***: Numerical simulation, concrete armor unit, fracture model, combined finite-discrete element method, Dolos, Core-Loc

# 1 Introduction

Rubble-mound coastal structures are widely used for breakwaters in harbour construction and for revetments to protect shorelines. They rely on massive randomly placed concrete units (or huge pieces of rock known collectively as armourstone). These are placed on the seaward slopes in granular layers to withstand and dissipate the forces of the expected storm waves. Breakwaters in deep water are typically covered by armour layers of concrete units and there are many different shapes of concrete unit designed to be used in different ways, e.g. as double layers or single layers (CIRIA/CUR/CETMEF, 2007). The interlocking slender types of armour unit such as the Tetrapod and Dolos (plural Dolosse) which are placed randomly in double layers have largely given way to a new generation of interlocking concrete armour units that are chunkier and structurally more robust like the Core-Loc, Accropode I, Accropode II and Xbloc. These newer units are also placed randomly but in single layers and at high enough packing densities to greatly inhibit movement under wave action. However, some movement cannot be ruled out and so there remains a poorly understood risk posed by the potential for breakage of concrete units, especially with increasingly large units. For example, if under wave action units are still able to rock and collide, the larger are the colliding bodies, the higher are the dynamic tensile stresses generated.

Originally the design of concrete armour layers (armour unit size and shape, seaward slope, etc.) was based mainly on hydraulic stability criteria for a given design storm. This lacked consideration of the structural integrity of the units and the layer itself should breakages develop and progressively make the layer therefore unstable. In the nineteen seventies and eighties, however, severe breakages of concrete armour units were reported in several cases of breakwater failures (Burcharth, 1987), notably the Sines breakwater in Portugal. Therefore, the assessment of structural integrity of armour layers was understood to be an important and necessary factor in the design of such breakwaters.

Figure 1: Crescent City breakwater covered by Dolosse units, California, USA (after Myrick and Melby, 2005). The weight of each Dolos unit is 38.1 t. The red units are instrumented with internal strain gages for monitoring purpose.

The focus of this paper is to investigate the structural integrity of two types of unreinforced concrete armour unit: the Dolos unit and the Core-Loc unit. The decision not to reinforce is based on cost and the high corrosion cracking potential of seawater penetrating any reinforced concrete. Among the various types of slender concrete armour units used on breakwaters, Dolosse units are a traditional and classical design which has been employed for decades in coastal engineering. A typical breakwater covered by Dolosse units at Crescent City, California, USA is show in Figure 1. Because of the long history of using Dolosse units, during which several breakwater failure cases occurred, a large number of research studies have been devoted to the structural stability of the Dolos unit. One main research area is monitoring at breakwater sites that have used Dolosse units. For example, Kendall and Melby (1992), Appleton et al. (1996), and Myrick and Melby (2005) have all contributed towards a comprehensive monitoring study of Crescent City breakwater, California, USA. Another main research area is the combination of analytical approaches with laboratory experiments.

Burcharth (1981b), Terao (1982), Zwamborn and Scholtz (1986, 1988), Lin et al. (1986), and Hall et al. (1987) investigated the structural response of Dolosse units under different dynamic loading conditions by combining analytical and experimental methods. All these study methods led to a better understanding of how these interlocking Dolosse units work in reality and what might be done to improve their design (Burcharth, 1983; Timco, 1984; Burcharth et al. 1990). For example, Burcharth (1981b) systematically tested the relation between sizes of full-scale Dolosse units and their dynamic strength, and investigated the fracture patterns under different dynamic loading conditions, as well as the influence of reinforcement, concrete properties and surface cracks on the strength of the units. The data from Burcharth's work (1981b) are used to validate the numerical model in this paper. Several important studies of the structural response of Core-Loc units under disturbance were conducted by Melby and co-workers, e.g. see Melby (2002). Their work tested the strength of Core-Loc units in laboratory conditions and used the finite element method (FEM) for numerical simulations of individual units to further investigate the stresses that might be expected in extreme cases of loading.

One developing area that continues to attract more and more interest is the use of numerical modelling programs to simulate the structural integrity of concrete units such as Dolosse units. The numerical modelling approach has many advantages for coastal engineers. One is that it can significantly reduce the cost and labour needed for physical experiments. Another is that numerical modelling can accurately control loading and set up extreme conditions representative of full-scale units, which would help investigate complicated conditions that are difficult to set up in laboratories, and which are needed to test the strength limits of Dolosse units of different design sizes. Tedesco et al. (1987, 1991, 1992), Scott et al. (1990), and Rosson and Tedesco (1992, 1993) have all applied FEM-based numerical programs to simulate the structural response of the Dolos unit under static and dynamic loading conditions. They plotted time histories of stresses at several key points on Dolosse units and derived iso-stress curves for Dolosse units of different sizes. Although many insights were obtained by examining the stress fields in Dolosse units, and many other unit types have since been subjected to similar FEM stress analysis, these modelling tools cannot explicitly initiate and develop discrete fractures. Furthermore, without the multi-body capability of the discrete element method (DEM), their FEM codes alone cannot capture the multi-body loading of all the contacts existing in a real granular armour layer system of interlocking units.

The combined finite-discrete element method (FEMDEM) appears uniquely well-suited as a means to study armour layer behaviour and this has led to considerable advances in the ability of numerical methods to examine the latest generation of single layer unit systems such as Core-Loc. The FEMDEM method uses FEM formulation to simulate continuum deformation and DEM formulation for multi-body interaction. A source of references and progress towards this goal was presented in Latham et al. (2013), where full scale Core-Loc armour layers built with 242 units, each of 8 $m^3$ concrete volume, were successfully simulated using a ‘rigid’ behaviour version of the FEMDEM program under static (and dry) conditions; contact force distributions corresponding to a range of different packing densities (one of the key parameters in construction specification), were evaluated numerically in their study. However, in this context, while considerable advances have been made in the numerical construction of realistic armour layers, significant progress in capturing the detailed geometry together with internal stresses and the modelling of fracture has presented a considerable challenge because of the need to develop a robust three-dimensional fracture model in FEMDEM. The new fracture model of the deformable FEMDEM program recently developed by the first author is used here to model internal dynamic stresses and fracture in armour units. As it uses more CPU than the rigid version of the program, it will be illustrated in this paper with just a few complex-shaped bodies.

Table 1: Types and origins of loads on armour units (after Burcharth, 1981a)

| Types of loads | Origins of loads | |
|---|---|---|
| **Static** | *Weight of units* | |
| | *Prestressing* | Settlement of underlayers |
| | | Wedge effect and arching due to movements under dynamic loads |
| **Dynamic** | *Impact* | Rocking/rolling of units |
| | | Missiles of broken units |
| | | Placing during construction |
| | *Pulsating* | Gradually varying wave force including slamming |
| | | Earthquake |
| **Abrasion** | *Suspended material* | |
| **Thermal** | *Stresses due to temperature differences during hardening processes* | |
| | *Freeze-thaw* | |
| **Chemical** | *Corrosion of reinforcement* | |
| | *Sulphate reactions, etc.* | |

One key aspect to be addressed before numerical modelling can be applied in design work is to define and find a means of applying the wave loading conditions that units are exposed to. According to previous research, there are five main types of loads acting on armour units (Burcharth, 1981a; Howell, 1988; Burcharth et al., 1991), which are listed in Table 1. The complexity of the *in situ* loading conditions makes it very difficult even impossible to accurately represent reality in physical experiments and numerical simulations. Therefore, some simplified loading conditions are derived from reality to represent typical loading conditions. For example, the impact loading may occur because of rocking and rolling of armour units subject to wave-induced forces, which can be simplified by drop tests in a laboratory environment; or the impact loading may occur when pieces of broken units (missiles) are thrown against other units by the waves, which can be simplified into pendulum type tests in a laboratory environment. It is worth mentioning that even a small motion of an armour unit can cause it to suffer severe breakages. This is because the mass of the unit is often made very large (for hydraulic stability) and hence impacts can involve very large forces. These create high amplitude tensile stress waves sufficient to exceed the invariably unreinforced concrete strength, which after some years after construction typically have mean values of 3.5 – 4.3 MPa (Franco et al., 2000).

The research objective of this paper is to apply the new three-dimensional fracture model within the FEMDEM program to investigate the structural integrity of concrete armour units under dynamic and extreme loading conditions. The focus is on the numerical simulation of fracturing behaviour in complex stress fields and the interaction between multiple bodies. First, The newly developed three-dimensional fracture model in the context of the FEMDEM method is described in Section 2. Next in Section 3, Dolosse units are simulated in two tests, the drop test and the pendulum test, to explore the structural integrity of the Dolos unit and its vulnerability to fracturing; and the results are compared with Burcharth's experiments (1981b) as a means of validating the code's accuracy. Further to the code validation presented in another paper (in preparation for publication), and having validated the code in Section 3 specifically for the fracturing of Dolosse units under dynamic loading, in Section 4, an application to a much more complex problem is presented. Core-Loc units are simulated under an imaginary extreme loading condition, which gives some insights into a worst case failure scenario. The potential that the technology has to capture the complex physical behaviour of armour layers including how they may progressively break up is shown.

## 2 Three-dimensional fracture model in the context of the combined finite-discrete element method

The combined finite-discrete element method (FEMDEM) was first pioneered by Munjiza in the nineteen nineties, later becoming established with a text book(Munjiza 2004), and then further developed by several research groups all around the world. One of the main contributions to the development of the three-dimensional FEMDEM program is made in the AMCG group (Applied Modelling and Computation Group) at Imperial College London (Xiang et al., 2009). More importantly, a three-dimensional fracture model has been developed which is able to simulate the whole fracturing process, including both tensile and shear fracture initiation and propagation and post-peak interaction between discrete fracture surfaces, for quasi-brittle materials, e.g. rock and unreinforced concrete. A detailed paper describing the three-dimensional fracture model including algorithms and validation tests is in preparation for publication, and a brief description is given below.

## 2.1 Overall algorithm of three-dimensional fracturing simulation

In three-dimensional fracturing simulations in the context of the FEMDEM method, the whole domain is treated as a multi-body system. Each discrete body is a single discrete element, which is further discretised into finite element mesh. The finite element formulation is used to simulate continuum behaviour on finite element mesh for each discrete body, which includes the calculation of strain and stress in finite elements. The discrete element formulation is used to simulate discontinuum behaviour (contact interaction) between discrete bodies, which means the calculation of contact force and the distribution of contact force to finite element nodes. The fracture model links the finite element formulation with the discrete element formulation. For each intact discrete body, before fracture initiation, the stresses are calculated by the finite element formulation; if the stress state meets the failure criterion, a discrete fracture will form and the discontinuous interaction between discrete fracture surfaces will be modelled explicitly by the contact algorithms in the discrete element formulation; therefore, the whole process of transition from continuum to discontinuum can be accurately captured. Figure 2 shows the overall algorithm for three-dimensional fracturing simulation based on the FEMDEM method.

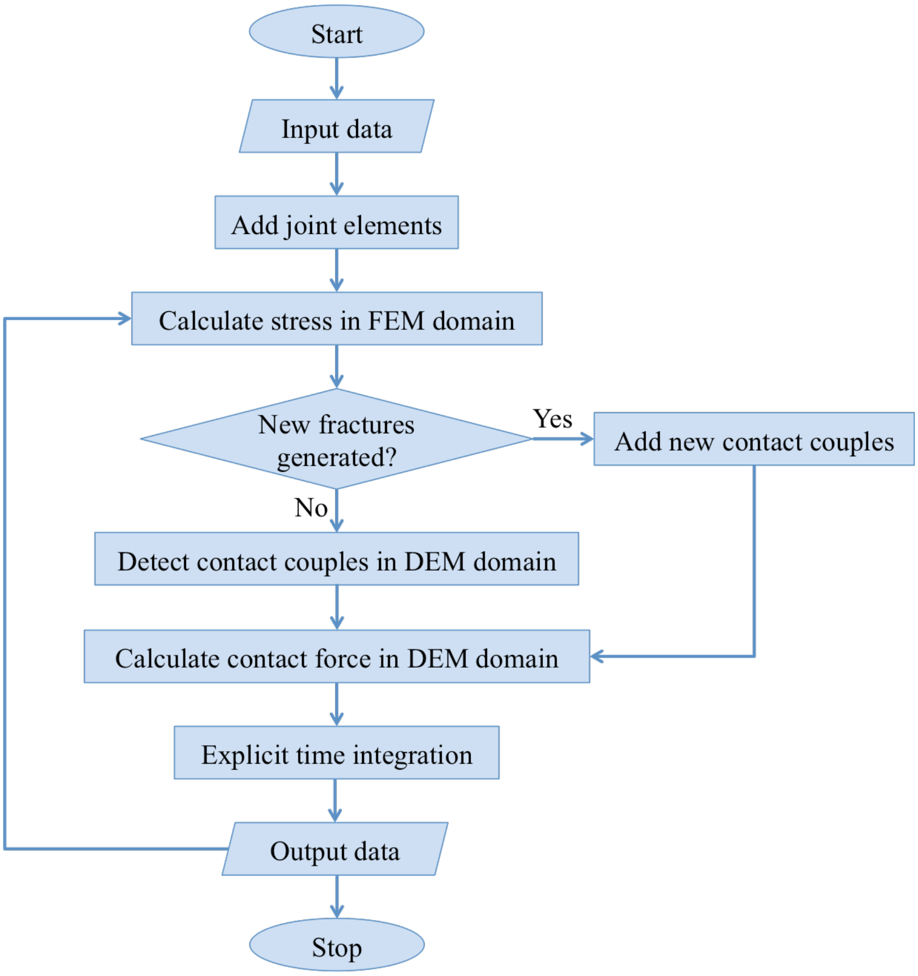

Figure 2: Flowchart of three-dimensional fracturing simulation.

## 2.2 Fracture initiation and propagation

### 2.2.1 Joint element

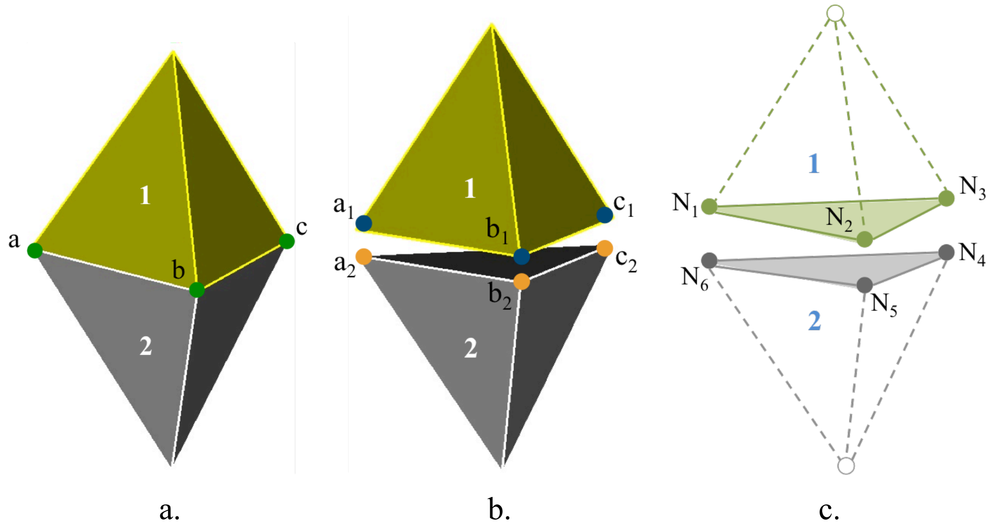

Figure 3: Joint element topology.

The three-dimensional fracture model works on a modified 4-node tetrahedral element mesh. First, the domain is discretised using 4-node tetrahedral elements; then special 6-node joint elements are inserted between tetrahedral elements. Take a mesh of two tetrahedral elements for example, the procedure of inserting a joint element and its topology is shown in Figure 3. Figure 3a shows two adjacent tetrahedral elements 1 and 2 sharing three nodes $a$, $b$ and $c$ in an original continuous finite element mesh. First these two tetrahedral elements are detached (Figure 3b), so they do not share nodes any more; all three nodes $a$, $b$ and $c$ are being duplicated, so new nodes $a_1$, $b_1$ and $c_1$ belong to element 1, and $a_2$, $b_2$ and $c_2$ belong to element 2. It should be noted that at this initial pre-processing stage, there is no deformation caused by any form of loading in the domain, so every pair of nodes $a_1$-$a_2$, $b_1$-$b_2$ and $c_1$-$c_2$ occupy the same position but with different node numbers in the mesh topology. Then the duplicated nodes $a_1$, $b_1$, $c_1$, $c_2$, $b_2$ and $a_2$ are renumbered as $N_1 \sim N_6$, and a 6-node joint element with nodes $N_1 \sim N_6$ is inserted (Figure 3c) between tetrahedral elements 1 and 2.

### 2.2.2 Constitutive model with failure criterion

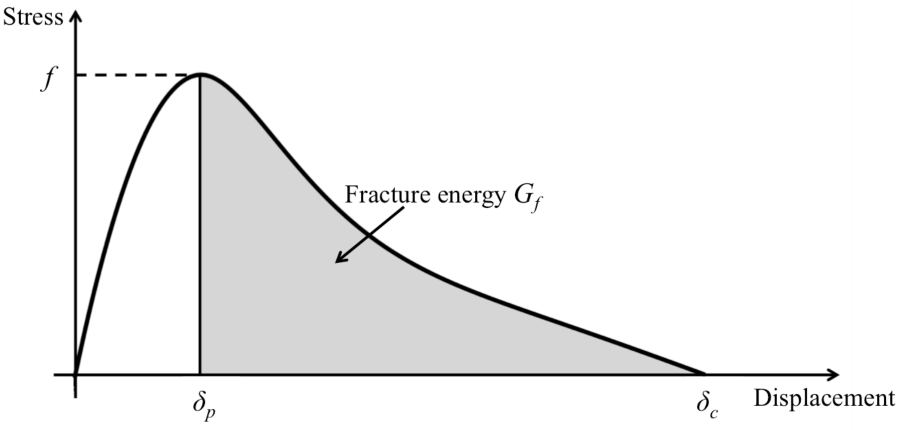

Figure 4: Constitutive model for joint element.

The constitutive model used in the three-dimensional fracture model is similar to the combined single and smeared crack model proposed by Munjiza et al. (1999). The normal stress $\sigma$ and the shear stress $\tau$, corresponding to the normal displacement $\delta_n$ and the shear displacement $\delta_s$ between triangular surfaces $N_1N_2N_3$ and $N_4N_5N_6$ (Figure 3c), respectively, are calculated according to a constitutive law as shown in Figure 4. It should be noted that this fracture model could also simulate fractures in materials other than the quasi-brittle ones considered here. As is shown in Figure 4, the stress-displacement constitutive model defined for joint elements is not restricted to small deformation, and stress can be calculated corresponding to any displacement value. Several key parameters in Figure 4 are explained below. The peak stress $f$ on this stress-displacement curve represents the material strength, so for normal stress $\sigma$, it means tensile strength $f_t$; and for shear stress $\tau$, it means shear strength $f_s$. The tensile strength $f_t$ is assumed to be a constant, while the shear strength $f_s$ is defined by the Mohr-Coulomb criterion with a tension cut-off (Equation 1),

$$f_s = \begin{cases} c - \sigma_n \tan\phi, & \text{if } \sigma_n < f_t \\ c - f_t \tan\phi, & \text{if } \sigma_n \geq f_t \end{cases} \tag{1}$$

where $c$ is cohesion, $\phi$ is internal friction angle, $\sigma_n$ is the normal stress acting perpendicular to the shear direction. Note here the engineering mechanics sign convention is used, so tensile stress is positive and compressive stress is negative. Fracture energy $G_f$ in

Figure 4 is a material property, which defines the energy needed for fracture surface to propagate per unit area. $\delta_p$ is the maximum elastic displacement corresponding to peak stress $f$ between two triangular surfaces $N_1N_2N_3$ and $N_4N_5N_6$ in a joint element, and $\delta_c$ is the critical displacement, at which the joint element fails.

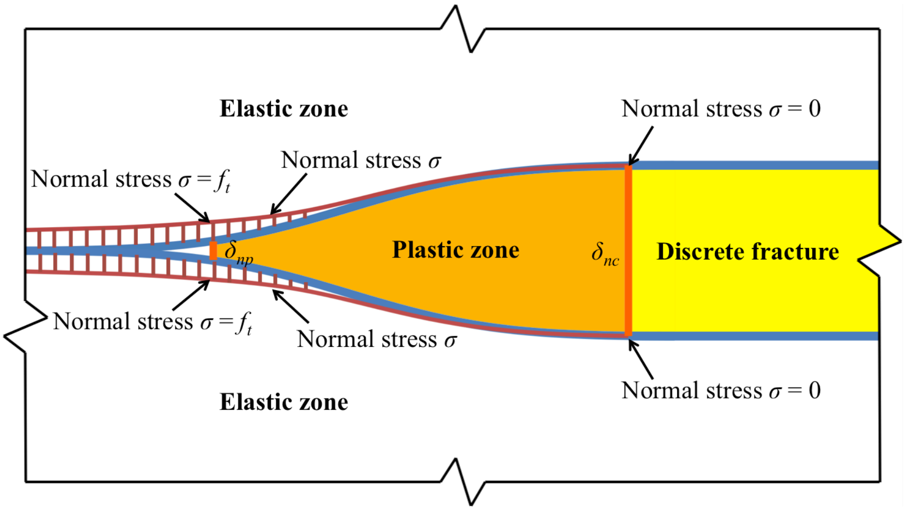

Figure 5: Transition from elastic zone to discrete fracture via plastic zone around a single mode I fracture tip. The short vertical red bars between the red line and the blue line represent the magnitudes of normal stress $\sigma$. Note that in a similar way, the shear stress $\tau$ can be illustrated by substituting parameters presented here as in the normal direction (with subscript $n$) with the corresponding parameters in the shear direction (with subscript $s$).

For a single mode I tensile fracture, for example, the physical meanings of $\delta_p$ and $\delta_c$ is illustrated in Figure 5. For this case, because it is pure tension, $\delta_p$ is represented by $\delta_{np}$ and $\delta_c$ is represented by $\delta_{nc}$. In Figure 5, the white area represents the continuum domain that is intact without any fractures; the light yellow area represents physically discrete fracture; the orange area between them is defined as plastic zone, which corresponds to the strain softening part ($\delta_{np} \sim \delta_{nc}$) in Figure 4. It is worth noting that in Figure 5 the short vertical red bars between the red line and the blue line represent the magnitudes of normal stress $\sigma$ in the joint elements. It can be seen from Figure 5 that $\delta_{np}$ represents the position, where the normal stress $\sigma$ in the joint element reaches its peak value (tensile strength $f_t$); ahead of this position (to the discrete fracture direction), the domain is at a strain softening stage (orange area), which means the normal stress $\sigma$ decreases from tensile strength $f_t$ to zero while the normal displacements $\delta_n$ increases from $\delta_{np}$ to $\delta_{nc}$. After this moment (when $\delta_n = \delta_{nc}$), this joint element will fail and the constitutive law is not applied to this failed joint element anymore. Instead, the interaction between the fracture walls will be counted as contact force, including normal compression and sliding friction, which is calculated by the contact algorithms. The detailed contact algorithms for the three-dimensional FEMDEM method can be found in Munjiza's book (2004).

The definitions of parameters in Figure 4, that are considered applicable to mass concrete are explained below. The normal stress $\sigma$ within three distinct displacement ranges can be defined as a function of normal displacement $\delta_n$ (Equation 2),

$$\sigma = \begin{cases} 2\dfrac{\delta_n}{\delta_{np}} f_t, & \text{if } \delta_n < 0 \\ \left[2\dfrac{\delta_n}{\delta_{np}} - \left(\dfrac{\delta_n}{\delta_{np}}\right)^2\right] f_t, & \text{if } 0 \le \delta_n \le \delta_{np} \\ z f_t, & \text{if } \delta_{np} < \delta_n \le \delta_{nc} \end{cases} \tag{2}$$

where $\delta_{np}$ is the maximum elastic displacement in the normal direction, $\delta_{nc}$ is the critical displacement at failure in the normal direction, $z$ is a heuristic softening parameter by curve fitting using experiment data of concrete in tension (Xian et al., 1991; Munjiza et al., 1999), which is calculated using Equation 3,

$$z = \left[1 - \frac{a+b-1}{a+b} \exp\left(D \frac{a+bc}{(a+b)(1-a-b)}\right)\right]\left[a(1-D) + b(1-D)^c\right] \tag{3}$$

where $a$, $b$ and $c$ are material properties derived from experiment data, and $D$ is a parameter calculated considering both normal displacement $\delta_n$ and shear displacement $\delta_s$, which is given by Equation 4,

$$D = \begin{cases} \dfrac{\delta_n - \delta_{np}}{\delta_{nc} - \delta_{np}}, & \text{if } \delta_{np} < \delta_n < \delta_{nc} \text{ and } \delta_s < \delta_{sp} \\ \dfrac{\delta_s - \delta_{sp}}{\delta_{sc} - \delta_{sp}}, & \text{if } \delta_{sp} < \delta_s < \delta_{sc} \text{ and } \delta_n < \delta_{np} \\ \sqrt{\left(\dfrac{\delta_n - \delta_{np}}{\delta_{nc} - \delta_{np}}\right)^2 + \left(\dfrac{\delta_s - \delta_{sp}}{\delta_{sc} - \delta_{sp}}\right)^2}, & \text{if } \delta_{np} < \delta_n < \delta_{nc} \text{ and } \delta_{sp} < \delta_s < \delta_{sc} \\ 1, & \text{if } \delta_n \geq \delta_{nc} \text{ or } \delta_s \geq \delta_{sc} \\ 0, & \text{otherwise} \end{cases} \tag{4}$$

where $\delta_{sp}$ is the maximum elastic displacement in the shear direction, $\delta_{sc}$ is the critical displacement at failure in the shear direction, and $\delta_{np}$ and $\delta_{nc}$ have the same meanings as in Equation 2. In a similar way, the shear stress $\tau$ can be calculated by substituting normal displacement $\delta_n$ with shear displacement $\delta_s$, and other parameters in the normal direction (with subscript $n$) with the corresponding parameters in the shear direction (with subscript $s$) in Equation 2.

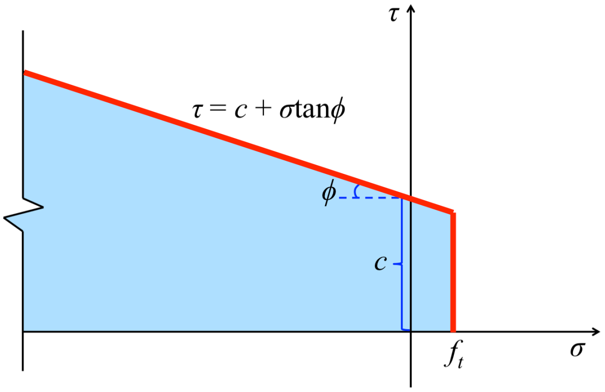

Figure 6: A Mohr-Coulomb failure criterion with a tension cut-off. $c$ is cohesion, $\phi$ is internal friction angle, $f_t$ is tensile strength, $\tau$ is shear stress in joint element, and $\sigma$ is normal stress in joint element. Note the engineering mechanics sign convention is used here, so tensile stress is positive and compressive stress is negative.

The failure criterion used in the three-dimensional fracture model is a Mohr-Coulomb failure criterion with a tension cut-off (as shown in Figure 6). It is a stress-based failure criterion involving stress components both in the normal direction $\sigma$ and in the shear direction $\tau$. A tension cut-off $\sigma = f_t$ is added to a classic linear Mohr-Coulomb failure envelope to modify the unrealistic tensile failure given by the original Mohr-Coulomb failure envelope. It can be seen from Figure 6 that under the failure envelope (blue area), the material is in a safe state of stress. Once the stress state in a joint element reaches the failure envelope (red line), the two surfaces $N_1N_2N_3$ and $N_4N_5N_6$ of the joint element (Figure 3c) will physically detach, and a fracture with two discrete surfaces $N_1N_2N_3$ and $N_4N_5N_6$ will form. It should be noted that the three-dimensional fracture model used in this paper is based on a fixed mesh, so fractures only propagate along tetrahedral element boundaries. A typical fracture surface obtained in such fixed-mesh-based three-dimensional fracturing simulations is shown in Figure 7.

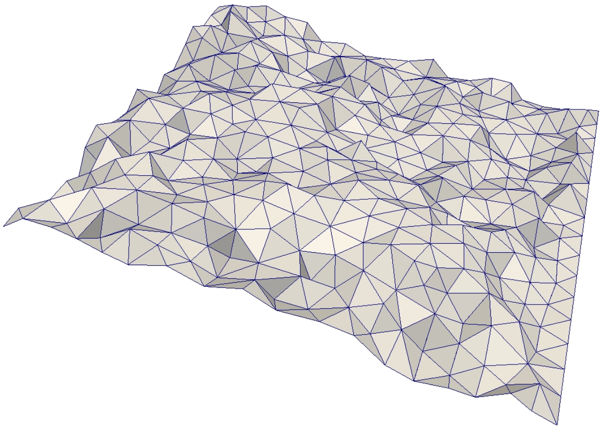

Figure 7: A typical fracture surface obtained by using the three-dimensional fracture model based on fixed mesh.

## 2.3 Discretised equilibrium equations

### 2.3.1 Governing equations

In the three-dimensional fracturing simulations, the domain is discretised by 4-node tetrahedral elements and 6-node joint elements. The motions of element nodes are governed by internal forces and external forces acting on them. The governing equation for every individual node is given as

$$m_i \dot{\mathbf{v}}_i + \mathbf{f}_{int} = \mathbf{f}_{ext} \tag{5}$$

where $m_i$ is the mass of node $i$, $\dot{\mathbf{v}}_i$ is the acceleration vector of node $i$, $\mathbf{f}_{int}$ is the internal force vector of node $i$, $\mathbf{f}_{ext}$ is the external force vector of node $i$. In three-dimensional fracturing simulations, the internal force $\mathbf{f}_{int}$ is calculated from stresses of tetrahedral elements; the external force $\mathbf{f}_{ext}$ includes three parts, and is calculated as

$$\mathbf{f}_{ext} = \mathbf{f}_{joint} + \mathbf{f}_{contact} + \mathbf{f}_{load} \tag{6}$$

where $\mathbf{f}_{joint}$ is the external force vector contributed by the deformation in joint elements, $\mathbf{f}_{contact}$ is the external force vector contributed by the contact interaction, including normal compression and sliding friction, $\mathbf{f}_{load}$ is the external force vector contributed by external loading, such as body force and surface traction.

### 2.3.2 Explicit time integration

A forward Euler method (FE) is used in the three-dimensional fracturing simulations for explicit time integration. After the calculation of all the parts contributing to the nodal force in Equation 5, the unbalance force $\mathbf{f}_{unbalance}$ can be calculated as

$$\mathbf{f}_{unbalance} = \mathbf{f}_{ext} - \mathbf{f}_{int} \tag{7}$$

Then the acceleration and velocity at nodes are calculated as

$$\dot{\mathbf{v}}_t = \frac{\mathbf{f}_{ext} - \mathbf{f}_{int}}{m_i} \tag{8}$$

$$\mathbf{v}_{t+1} = \mathbf{v}_t + \dot{\mathbf{v}}_t \Delta t \tag{9}$$

where $\dot{\mathbf{v}}_t$ is the acceleration vector of node $i$ at the current time-step $t$, $\mathbf{v}_t$ is the velocity vector of node $i$ at the current time-step $t$, $\mathbf{v}_{t+1}$ is the velocity vector of node $i$ at the next time-step $t+1$, $\mathbf{f}_{ext}$ is the external force vector for node $i$, $\mathbf{f}_{int}$ is the internal force vector for node $i$, $m_i$ is the mass of node $i$, and $\Delta t$ is the time-step. Based on the obtained velocity, the node coordinates can be updated,

$$\mathbf{x}_{t+1} = \mathbf{x}_t + \mathbf{v}_{t+1} \Delta t \tag{10}$$

where $\mathbf{x}_t$ is the coordinate vector of node $i$ at the current time-step $t$, $\mathbf{x}_{t+1}$ is the coordinate vector of node $i$ at the next time-step $t+1$.

The choice of time-step is important for the numerical stability of the three-dimensional fracturing simulations, and both the FEM and DEM stability requirements should be considered. According to the FEM stability requirement, a time-step corresponding to approximately one-tenth of the time required for the stress wave to travel through a tetrahedral element is used. Based on the speed of stress wave propagating in a solid rod (Kolsky, 1964), the time-step required by FEM stability $\Delta t_{FEM}$ is estimated as

$$\Delta t_{FEM} \sim \frac{h}{10}\sqrt{\frac{\rho}{E}} \tag{11}$$

where $\rho$ is the density, $E$ is the Young's modulus, and $h$ is the minimum length of the edges of tetrahedral elements. According to the DEM stability requirement (Tsuji et al., 1993), which is based on the oscillation period of contacting discrete particle motion, the time-step required by DEM stability $\Delta t_{DEM}$ is estimated as

$$\Delta t_{DEM} \sim \frac{\pi}{5}\sqrt{\frac{m}{k}} \tag{12}$$

where $m$ is the minimum mass of one single tetrahedral element, and $k$ is the contact stiffness between tetrahedral elements (unit: N/m), which is a material property. The ultimate time-step $\Delta t$ used in the numerical simulations is the smaller value between $\Delta t_{FEM}$ and $\Delta t_{DEM}$,

$$\Delta t = \min\left\{\Delta t_{FEM}, \Delta t_{DEM}\right\} \tag{13}$$

## 3 Simulation of Dolosse units under dynamic loading conditions

A typical Dolos unit (shown in Figure 8) consists of two flukes, which are oriented at right angles to each other, and an intermediate stem, or trunk, which connects the two flukes. The dimensions of the Dolosse units simulated in this paper are shown in Figure 8, which are smaller than the dimensions of prototype Dolosse units employed in breakwater construction. It is worth noting that Burcharth (1981b) tested full-scale Dolosse units in physical experiments; here the dimensions are scaled down, but the ratios $a/H$, $b/H$ and $c/H$ are kept the same as the original units. This choice is based on the consideration of a balance between high accuracy and affordable CPU time. On the one hand, high accuracy is required to compare numerical simulations with physical experiments, so element size should be small enough to correctly represent the stress gradient in the plastic zone around a fracture tip. On the other hand, refined element size in three dimensions leads to a significant increase in the total element number, which will prolong the CPU time considerably. Therefore, to achieve a balance between high accuracy and affordable CPU time, the dimensions of simulated Dolosse units are scaled down from prototype dimensions. The three-dimensional FEMDEM code is currently being parallelised; once this is done, full-scale Dolosse units can be simulated with guaranteed high accuracy. In order to make these relatively small Dolosse units of normal concrete properties show breaking behaviour, the magnitude of dynamic loading is chosen to be relatively higher than the loading conditions acting on the larger Dolosse units used in Burcharth's original tests.

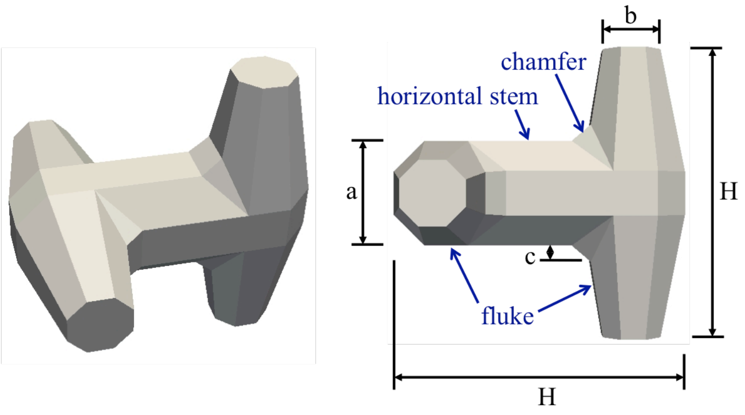

| Dimensions (mm) | | | | Weight (t) |
|---|---|---|---|---|
| H | a | b | c | |
| 1000 | 360 | 200 | 56 | 0.43 |

Figure 8: Geometry of Dolosse units, where *H*: total length of Dolos unit, *a*: width of stem, *b*: width of fluke at its end, *c*: width of chamfer. Note, in Burcharth's original units (1981b), $H$ = 2.32m.

In these tests, Dolosse units are simulated under two controllable dynamic loading conditions: a drop test (a hammer drop test) and a pendulum test. The drop test is designed to model the impact from wave-induced rocking of the units; the pendulum test is designed to model the impact from concrete pieces of broken units that are thrown against the units by waves.

The setup of the tests are similar to the ones used by Burcharth (1981b), who specially chose the supporting and loading conditions to ensure the units break in the stem, because in reality most damaged Dolosse units are fractured through the stem at a position close to the fluke. Burcharth's tests (1981b) involved repeated cycles of impacts, which are typically 6-8 strikes until the units break completely into two pieces. A notable difference is that the current material constitutive model in the three-dimensional FEMDEM code does not consider cyclic loading and fatigue of material. It should be noted that the plastic zone shown in Figure 5 is a simplification but not the complete concept of plasticity. The plastic zone is introduced to represent the plastically strained material at the tips of fractures, which is replaced by a zone of weakened bonding stresses in joint elements between tetrahedral elements. However, the loading/unloading is not considered in the current model, which means the loading history is not recorded. As a consequence, in the numerical simulations, a single strike is applied as the impact loading and only a partially through-going fracture is generated without breaking the units completely into two parts.

## 3.1 Drop tests

### 3.1.1 Test setup

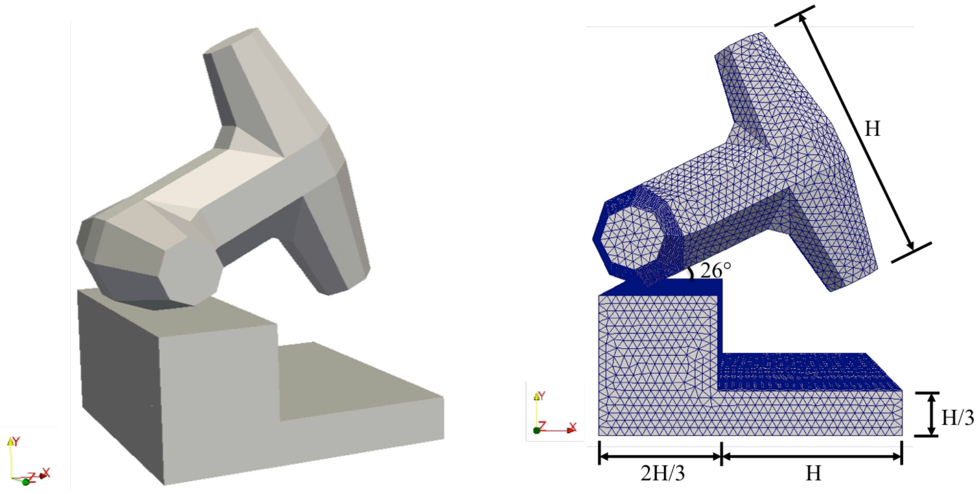

Figure 9: Drop test setup.

The drop test is designed to model the impact from wave-induced rocking of the units. There are two main types of drop tests: hammer type drop tests and free fall uncontrolled drop tests; here the drop test refers to the hammer type drop test. The setup of the drop test is shown in Figure 9. It should be noted that the simulated model, including the Dolos unit and the base, is scaled down from the original model in Burcharth’s test (1981b). In the test, first the Dolos unit is placed on a base in such a condition that it can stay stable without extra support. Then, the right end of the Dolos unit is lifted a certain height until the stem is at an angle of 26° to the horizontal plane (*xz*-plane), i.e. the rotation angle $\theta$ of the Dolos unit about the pivot axis is equal to 26°. Here the angle is specially chosen to ensure the Dolos unit can break (given the assumed representative concrete properties in Table 2) but not crush excessively. This is based on three considerations. First, from simulated tests of other rotation angles it is known that for smaller angles the Dolos unit does not break, and for larger angles the lower part of the right fluke crushes severely to small pieces. Second, the objective of this research is to investigate the breakages of Dolosse units, so loading conditions which do not cause breakages are excluded. Third, from a reality point of view, the Dolosse units are very unlikely to crush into small pieces even if they break. Lastly, the Dolos unit is released and drops from this initial position, so under gravity an impact loading condition will be generated once the lower end of the right fluke hits the base as a flat-on-flat impact. From the simulation results, it is known that applying an angle of 26° to this hammer type drop test on Dolosse units of $H$ = 1 m delivers comparable dynamic stress magnitudes to those generated in the tests of Burcharth (1981b) on the larger Dolosse units of $H$ = 2.32 m and rotation angle ~ 8°. Once the parallelisation of the three-dimensional FEMDEM code is done, the full-scale Dolosse units of $H$ = 2.32 m subject to exact loading conditions as in Burcharth's work (1981b) can be simulated with guaranteed high accuracy.

Velocity constrained boundary conditions are applied to the base. The bottom surface of the base is restrained in the $y$-direction; the two left-hand and right-hand surfaces are restrained in the $x$-direction; the two front and back surfaces are restrained in the $z$-direction. These conditions ensure there is no rigid body motion of the base. The fracture model is only applied to the Dolos unit and a viscoelastic constitutive model is applied to the base. Therefore, fracturing only occurs in the Dolos unit, and only viscoelastic deformation without fracturing is allowed to happen in the base. In reality, however, some of the impact energy would be absorbed by local inelastic deformation near the impact point in the base, so the simulated failure scenarios are conservative estimations of the dynamic response of Dolosse units. The acceleration of gravity $g$ is set to be 9.8 m/s$^{-2}$.

The type of material assigned to the Dolos unit and the base is unreinforced concrete. The same values are used for both the Dolos unit and the base (Table 2), however the difference is the Dolos unit is allowed to break but the base is only viscoelastically deformed without breaking. The concrete properties used in these tests are assumed to represent realistic Dolosse unit properties commonly employed in breakwater projects. The friction coefficient $\mu$ between the Dolos unit and the base is set to be 0.6.

Table 2: Material properties in drop test.

| Concrete properties | Values |
|---|---|
| Density $\rho$ (kg·m$^{-3}$) | 2340 |
| Young's modulus $E$ (GPa) | 26 |
| Poisson's ratio $\upsilon$ | 0.2 |
| Tensile strength $f_t$ (MPa) | 3.3 |
| Cohesion $c$ (MPa) | 16.5 |
| Internal friction angle $\phi$ (°) | 30 |
| Fracture energy $G_f$ (J·m$^{-2}$) | 50 |

The whole domain is meshed by unstructured 4-node tetrahedral elements, and the same mesh size is assigned to both the Dolos unit and the base (Figure 9). The average mesh size is approximately 2.9 cm. A total number of 170282 tetrahedral elements are generated. The Dolos unit consists of 67240 elements, and the base consists of 103042 elements. A time-step $\Delta t = 5 \times 10^{-8}$ s is used in the numerical simulations.

### 3.1.2 Results of intact Dolosse units

In this test, the Dolos unit is assumed to be perfectly intact, which means there are no pre-existing imperfections in the Dolos unit before applying the impact loading. A cut plane perpendicular to the $z$-direction and passing through the centre of the Dolos unit (shown in Figure 10) is made to show velocity and stress contours in this plane, and in the three-dimensional view of fractures, a semi-transparent colour scheme is adopted in order to show the fracture development inside the Dolos unit. From practical experience, it is known that under this loading condition the fractures are mostly tensile failures, so only stress contours of $\sigma_1$, which governs tensile failure, are shown here (Figure 11).

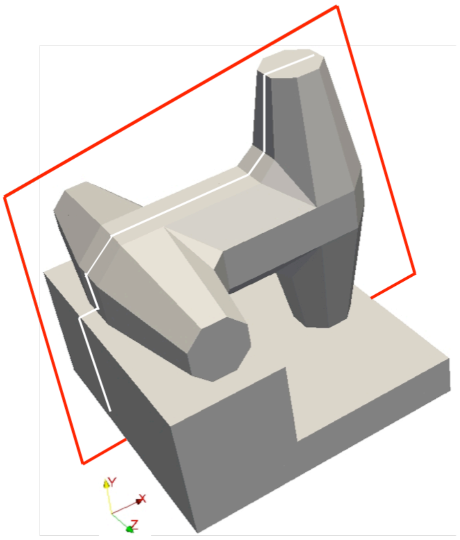

Figure 10: A cut plane perpendicular to the $z$-direction and passing through the centre of the Dolos unit.

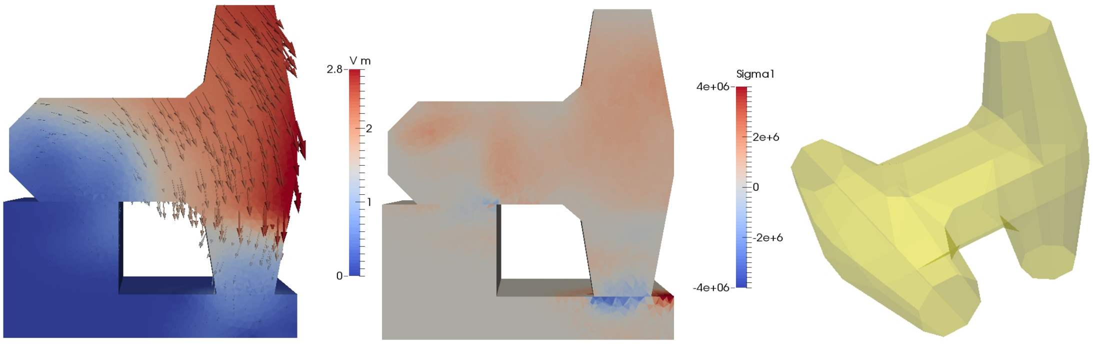

a. $t = 0.05$ ms.

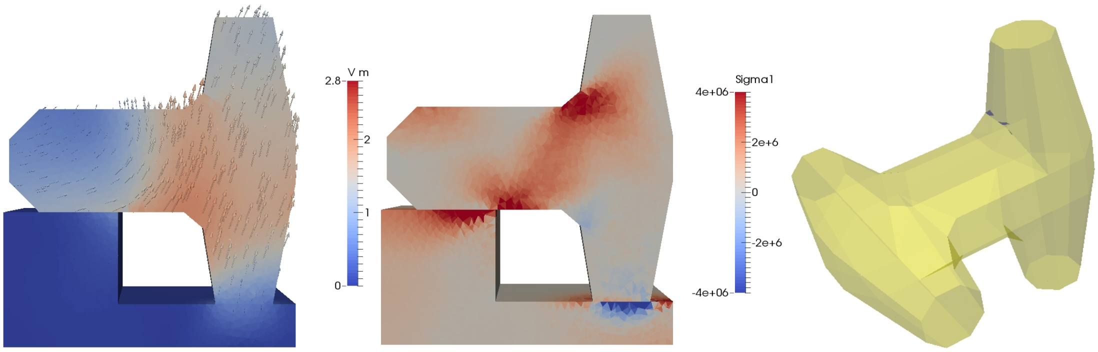

b. $t = 0.45$ ms.

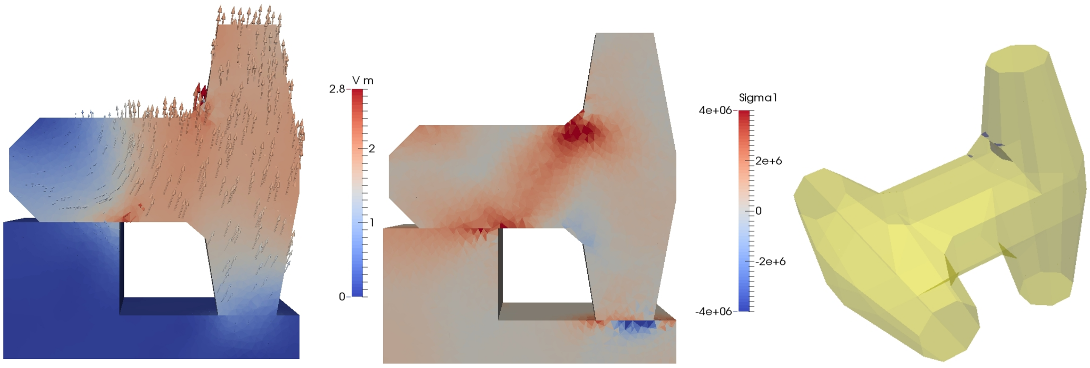

c. $t = 0.50$ ms.

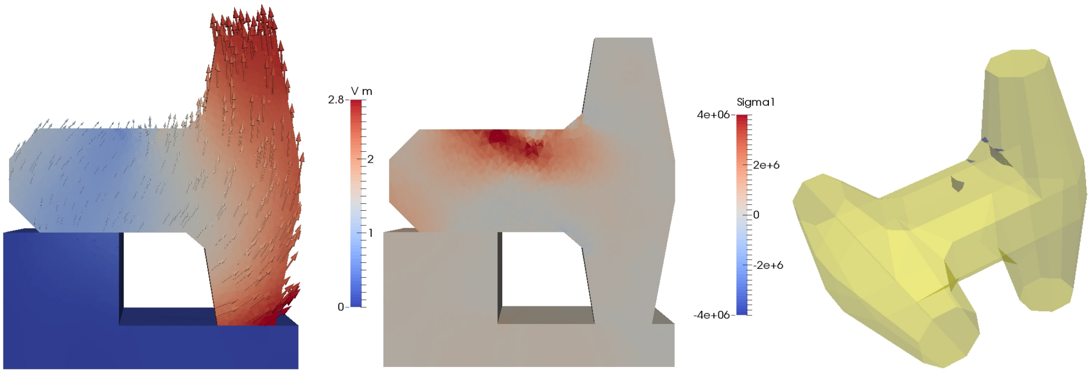

d. $t = 0.90$ ms.

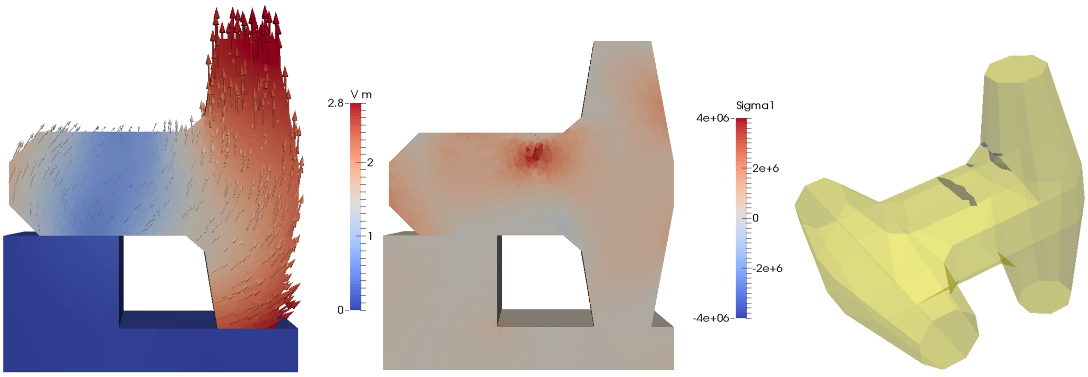

e. $t = 0.95$ ms.

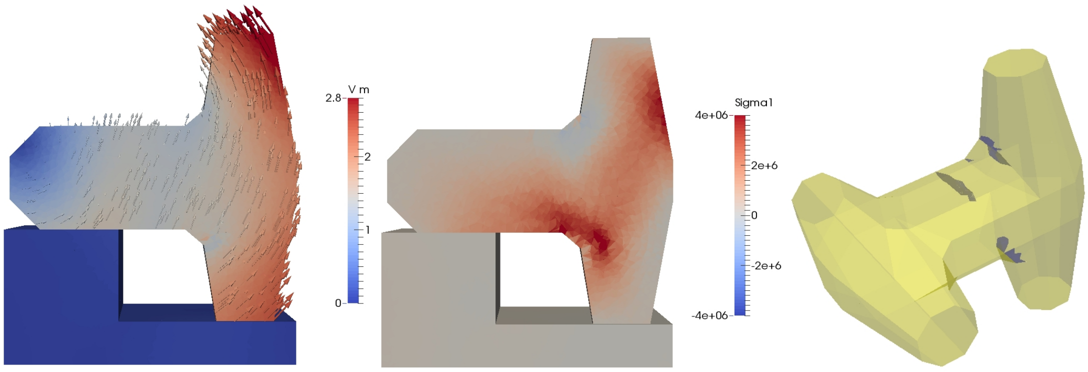

f. $t = 1.35$ ms.

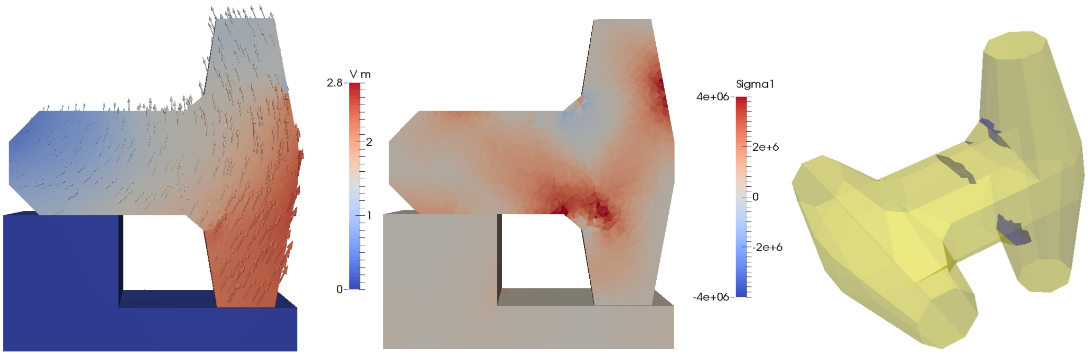

g. $t = 1.45$ ms.

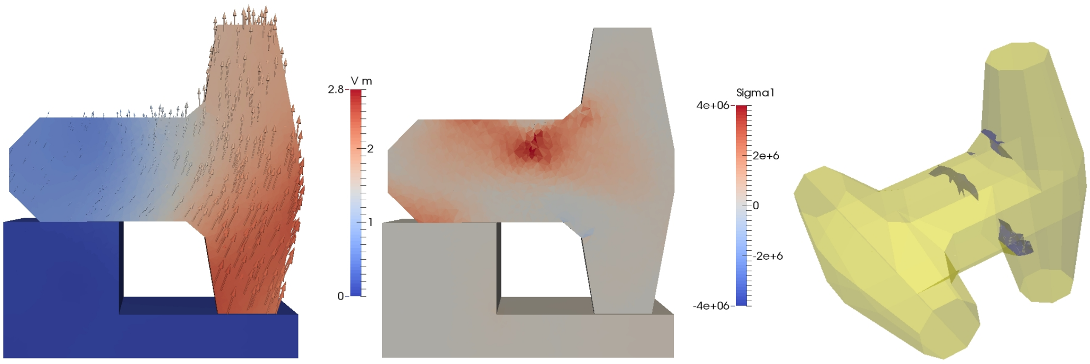

h. $t = 2.20$ ms.

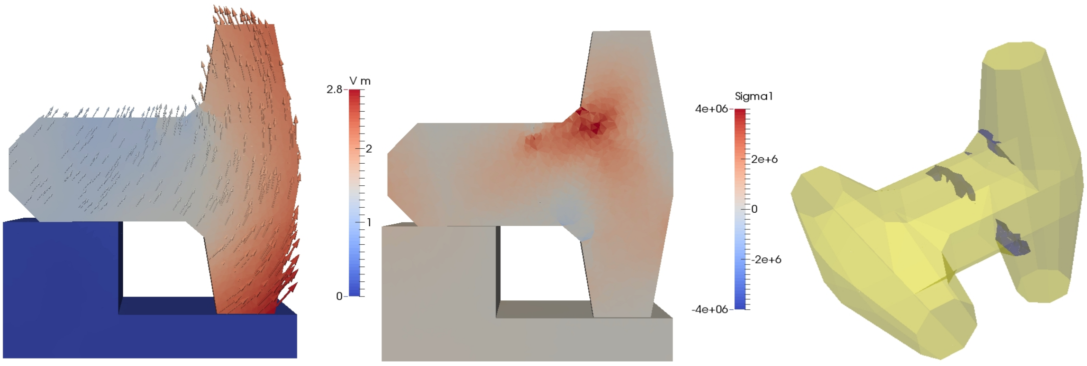

i. $t = 2.40$ ms.

Figure 11: Numerical simulation results of the drop test of a Dolos unit arranged in time sequence. Note that the time starts when the lower end of the right fluke hits the base. The left-hand column shows the velocity vector and magnitude in the cut plane perpendicular to the $z$-direction, where $v_m = \sqrt{\left(v_x^2 + v_y^2 + v_z^2\right)}$, and the unit of velocity is m·s$^{-1}$; the middle column shows the maximum principal stress $\sigma_1$ in the cut plane perpendicular to the $z$-direction, where tensile stress is positive, and compressive stress is negative, and the unit of stress is Pa; the right-hand column shows the three-dimensional fracture development in the Dolos unit, where the yellow colour represents the surfaces of the Dolos unit and the blue colour represents fracture surfaces.

During the drop test, shortly after the right fluke hits the base, there are two major stress concentrations in the Dolos unit (Figure 11b). One occurs in the upper stem-fluke corner (Figure 11b), which causes the first initiation of fractures in the Dolos unit. The other one is at the lower part of the stem where it touches the base, but the magnitude of stress concentration here is not large enough to initiate fractures. This stress concentration can be avoided by lowering the top left surface of the base and inserting a small plate between the left fluke of the Dolos unit and the base surface.

Then fractures further develop in the upper stem-fluke corner from the surface to the inside until the second stress concentration occurs in the middle of the top part of the stem (Figure 11d). It is worth noting that the stress concentration zone advancing the fracture tip moves as this fracture propagates inwards from the surface (see Figure 11e).

After some development, the fractures start initiating in the lower stem-fluke corner (Figure 11f), which means the next stress concentration in the Dolos unit occurs here. At the same time, another stress concentration occurs near the right boundary surface at the upper part of the right fluke, but the magnitude of stress here does not build up to the critical value for failure. After that, there is no new initiation of fractures in the Dolos unit; the only fracturing events are propagation of existing fractures. It can be seen that due to dynamic stress wave effects and fracture propagation, there are still stress concentrations in the Dolos unit, but the magnitudes are significantly reduced. Once the Dolos unit bounces off the base all the concentrated stresses are relieved and no more new fractures are formed in the Dolos unit (Figure 11i).

### 3.1.3 Results of Dolosse units with pre-existing surface cracks

It is known that surface cracks can exist in Dolosse units after casting even before the units are used in practice or subjected to dynamic tests (Burcharth 1981b, Figure 12). The generation of these surface cracks can be attributed to various reasons, such as the contraction of concrete during production stages and inappropriate placement of concrete units during construction. Considering these pre-existing surface cracks is essential to make numerical simulations as realistic as possible for practical engineering conditions. Therefore, several surface cracks are numerically introduced in the upper and lower stem-fluke corners of the Dolos unit before applying impact loading. A section cut by two parallel planes both perpendicular to the *x*-direction (shown in Figure 13) is made to show the fracture development inside the Dolos unit. The initial state of the pre-existing surface cracks is shown in Figure 14a. They extend from the surface at the chamfer connection running inside for approximately one element length (blue areas in Figure 14a).

The results of the drop test of the Dolos unit with pre-existing surface cracks are shown in Figure 14. It should be noted that in Figure 14 a section cut by two parallel planes both perpendicular to the *x*-direction (shown in Figure 13) is made to show the fracture development inside the Dolos unit. The motion and stress evolution of this Dolos unit with pre-existing surface cracks are very similar to the intact one, so only fracture development is shown here for comparison.

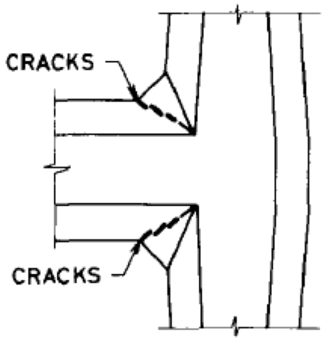

Figure 12: Typical surface cracks observed before testing in Dolosse units (after Burcharth, 1981b).

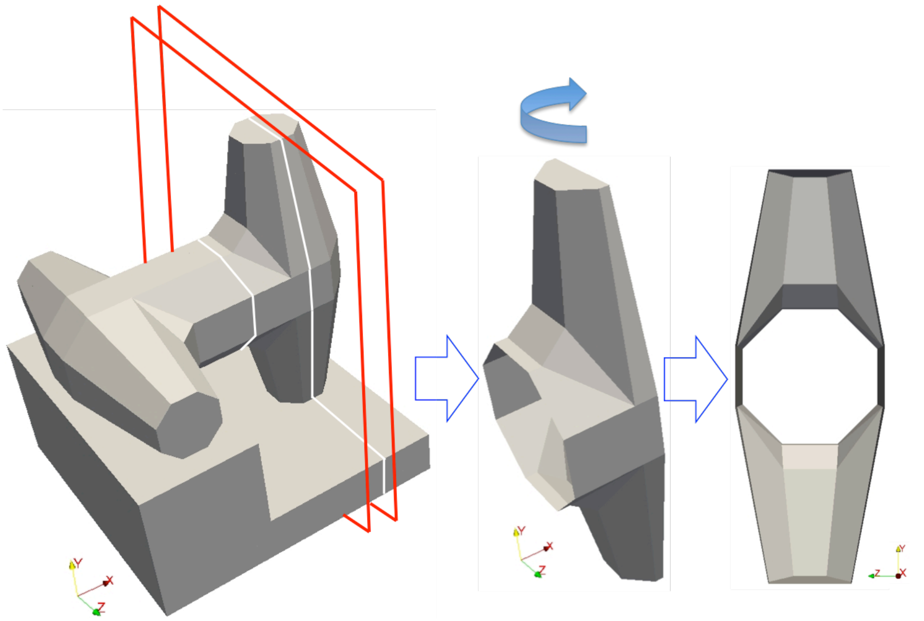

Figure 13: A section cut by two parallel planes both perpendicular to the *x*-direction to show the fracture development inside the Dolos unit. One cut plane is perpendicular to the *x*-direction and pass through the centre of the right fluke, and the other one is also perpendicular to the *x*-direction but pass through the stem.

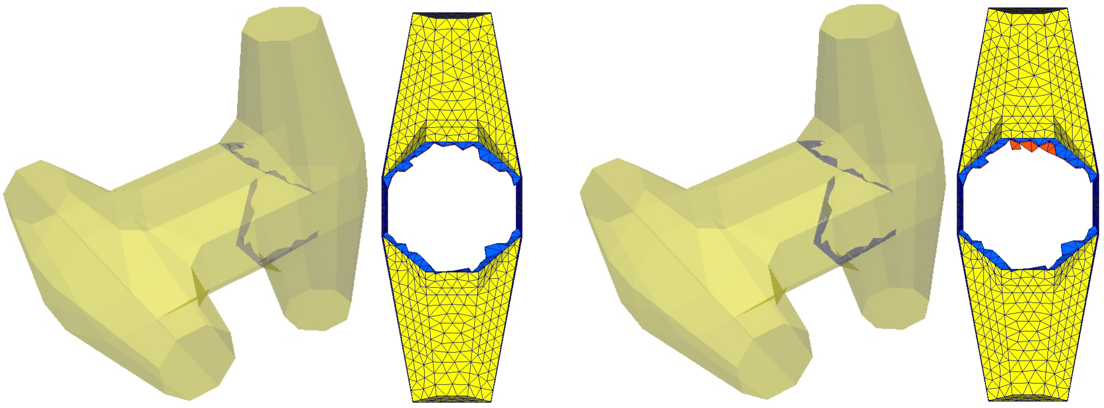

a. $t = 0$ ms.

b. $t = 0.50$ ms.

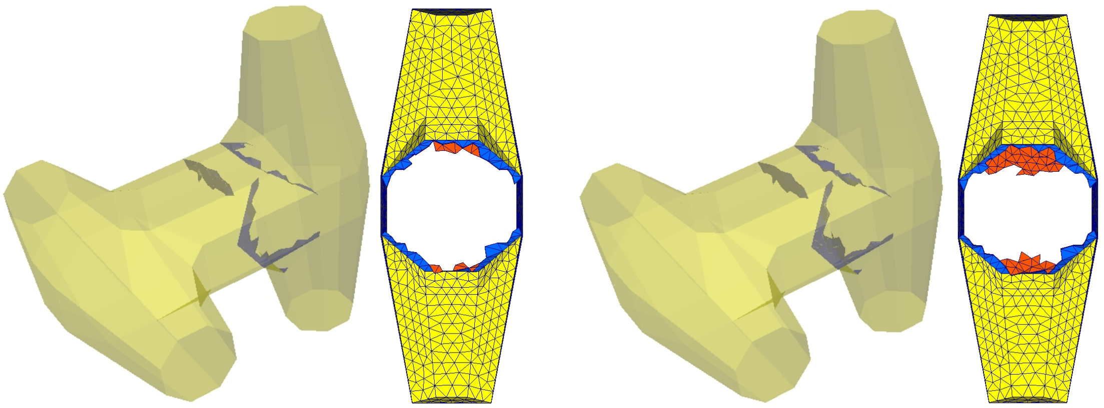

c. $t = 1.40$ ms.

d. $t = 2.45$ ms.

Figure 14: Fracture development in the drop test of a Dolos unit with pre-existing surface cracks arranged in time sequence. Note that the time starts when the lower end of the right fluke hits the base. In the three-dimensional semi-transparent view, the yellow colour represents surfaces of the Dolos unit, and the blue colour represents fracture surfaces, including both pre-existing surface cracks and newly formed fractures; in the cross-section view, the yellow colour represents surfaces of the Dolos unit, and the blue colour represents pre-existing surface cracks, and the orange colour represents newly formed fractures.

It can be seen from Figure 14 that fractures first initiate from the pre-existing surface crack tips in the upper stem-fluke corner (Figure 14b). After they propagate 1-2 element lengths, new fractures start to initiate in the middle of the top part of the stem and also develop from pre-existing surface crack tips in the lower stem-fluke corner (Figure 14c). The newly formed fractures in the lower stem-fluke corner only propagate for 2-3 element lengths and the final failure pattern (Figure 14d) shows that more new fractures of a greater areal extent are formed in the upper stem-fluke corner than in the lower corner.

## 3.2 Pendulum tests

### 3.2.1 Test setup

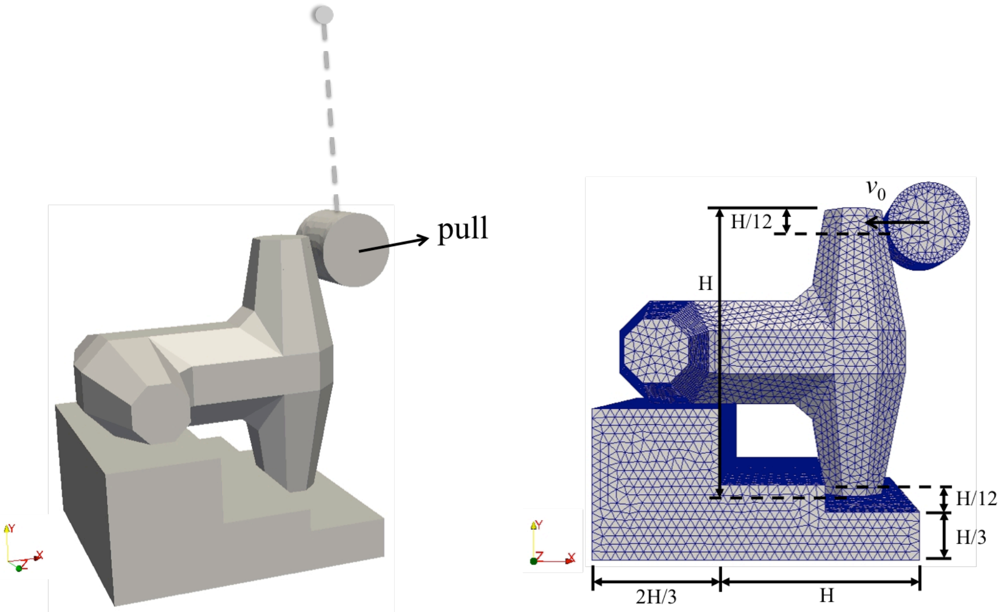

Figure 15: Pendulum test setup.

The pendulum test is designed to model the impact from concrete pieces of broken units that are thrown against the units by the waves. The setup of the pendulum test is shown in Figure 15. It should be noted that the simulated model, including the Dolos unit and the base, is scaled down from the original model in Burcharth's test (1981b). In this test, a Dolos unit is placed on a base in such a condition that it can stay stable without extra support. The base is similar to the base used in the drop tests (Figure 9), except a block with height equal to 1/12 $H$ is added to prevent the translational motion of the right fluke in the $x$-direction. A cylinder with length equal to diameter and weight equal to 1/5 of the Dolos unit is pulled back a certain height $h$ and then released to hit the unit. The impact point is 1/12 the length of the Dolos unit length $H$ measured from the end of the fluke. The position of the pivot and the length of the pendulum are chosen so that when the cylinder is at its resting equilibrium position, it just touches the surface of the Dolos unit. To ensure that the Dolosse units break but do not crush in the pendulum tests conducted with only one strike, the pulled back height $h$ of the cylinder is chosen to be 0.2 m, so when the cylinder hits the Dolos unit at its lowest position, the impact velocity $v_0$ equals 2 $\mathrm{m{\cdot}s^{-1}}$ (Equation 5). The acceleration of gravity $g$ is set to be 9.8 $\mathrm{m{\cdot}s^{-2}}$.

$$v_0 = \sqrt{2gh} \tag{14}$$

Velocity constrained boundary conditions are applied to the base similarly to the drop test. These conditions ensure that there is no rigid body motion of the base. The fracture model is only applied to the Dolos unit and the viscoelastic constitutive model is applied to the cylinder and the base. Therefore, fracturing only occurs in the Dolos unit, and only viscoelastic deformation without fracturing is allowed to happen in the cylinder and the base. As mentioned above, in reality, some of the impact energy would be dissipated by local inelastic deformation near the impact point both in the cylinder and in the base, so the simulated failure scenarios are conservative estimations of the dynamic response of Dolosse units.

The type of material assigned to the Dolos unit and the base is unreinforced concrete; the material of the cylinder is assumed to be steel. The material properties are shown in Table 3. Note that for the viscoelastic constitutive model applied to the cylinder, strength properties, i.e. tensile strength, cohesion, internal friction angle, and fracture energy, are not needed. Two values of friction coefficient $\mu$ are used in the test: $\mu$ is set to be 0.6 between the Dolos unit and the base (concrete-concrete contact), and 0.1 between the Dolos unit and the cylinder (concrete-steel contact).

Table 3: Material properties in pendulum test.

| Material types | Concrete | Steel |
|---|---|---|
| Density $\rho$ (kg·m$^{-3}$) | 2340 | 7850 |
| Young's modulus $E$ (GPa) | 26 | 200 |
| Poisson's ratio $\upsilon$ | 0.2 | 0.28 |
| Tensile strength $f_t$ (MPa) | 3.3 | ––– |
| Cohesion $c$ (MPa) | 16.5 | ––– |
| Internal friction angle $\phi$ (°) | 30 | ––– |
| Fracture energy $G_f$ (J·m$^{-2}$) | 50 | ––– |

The whole domain is meshed by unstructured 4-node tetrahedral elements, and the same mesh size is assigned to the Dolos unit, the cylinder, and the base (Figure 15). The average mesh size is approximately 2.9 cm. A total number of 187294 tetrahedral elements are generated. The Dolos unit consists of 66637 elements; the cylinder consists of 7104 elements; the base consists of 113553 elements. A time-step $\Delta t = 5 \times 10^{-8}$ s is used in the numerical simulations.

### 3.2.2 Results of intact Dolosse units

In the first test, the Dolos unit is assumed to be perfectly intact, which means there are no pre-existing imperfections in the Dolos unit before applying the impact loading. For results visualisation, a cut plane perpendicular to the $z$-direction and passing through the centre of the Dolos unit (shown in Figure 16a) is made to show velocity and stress contours in this plane, and a section cut by two parallel planes both perpendicular to the $x$-direction (shown in Figure 16b) is made to show the fracture development inside the Dolos unit. The results are shown in Figure 17. It is known that under this loading condition the fractures are mostly tensile failures so only stress contours of $\sigma_1$, which governs tensile failure, are shown here.

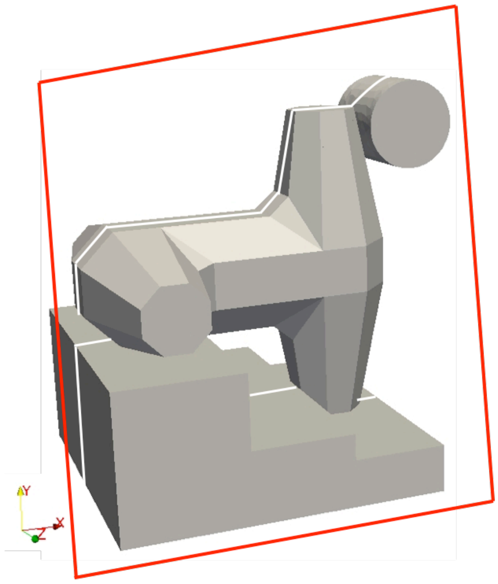

a. A cut plane perpendicular to the *z*-direction and pass through the centre of the Dolos unit.

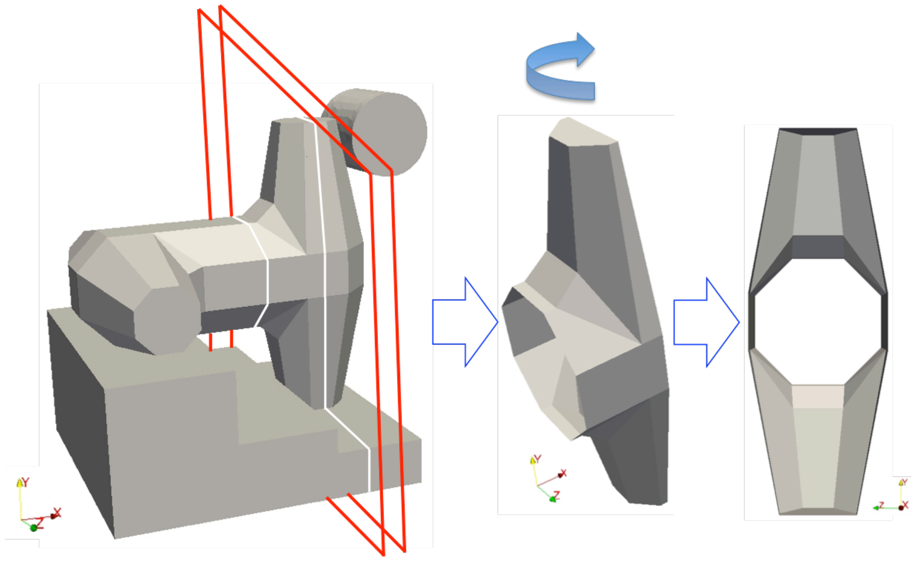

b. A section cut by two parallel planes both perpendicular to the *x*-direction to show the fracture development inside the Dolos unit. One cut plane is perpendicular to the *x*-direction and pass through the centre of the right fluke, and the other one is also perpendicular to the *x*-direction but pass through the stem.

Figure 16: Sections cut for result visualisation.

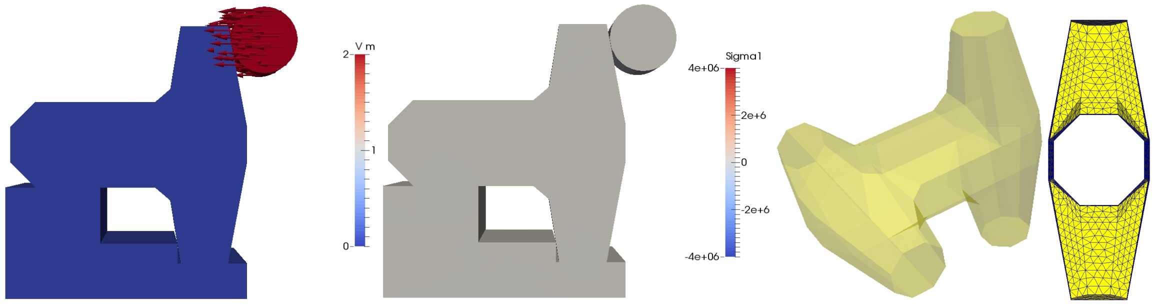

a. $t = 0$ ms.

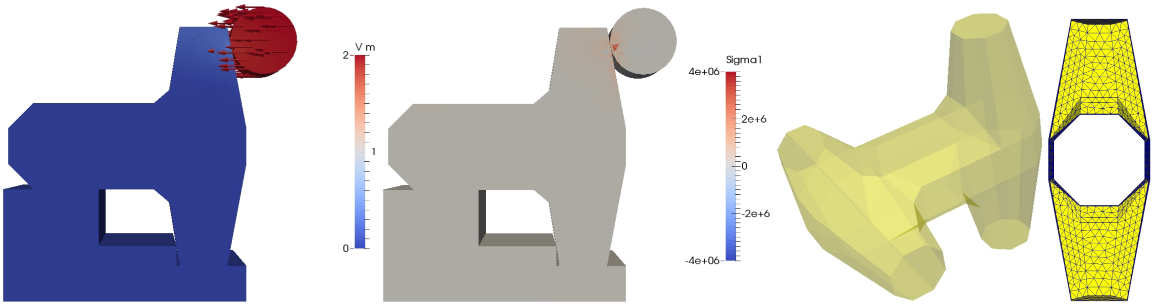

b. $t = 0.1$ ms.

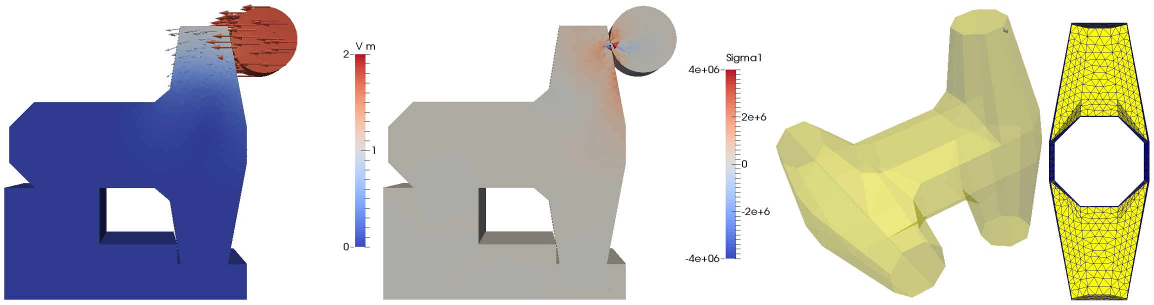

c. $t = 0.2$ ms.

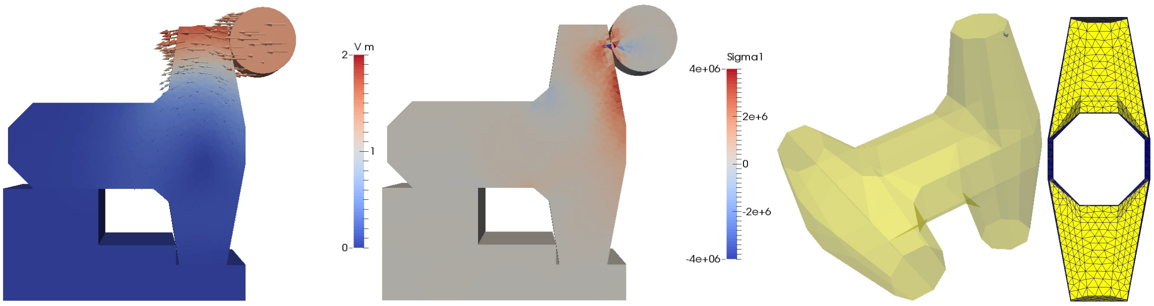

d. $t = 0.3$ ms.

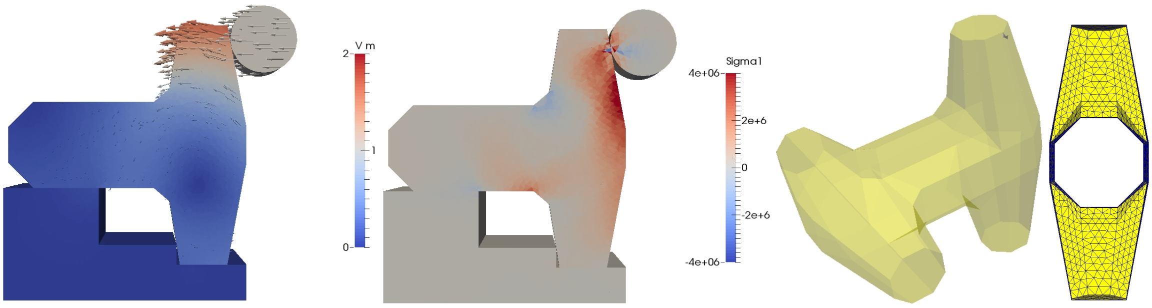

e. $t = 0.4$ ms.

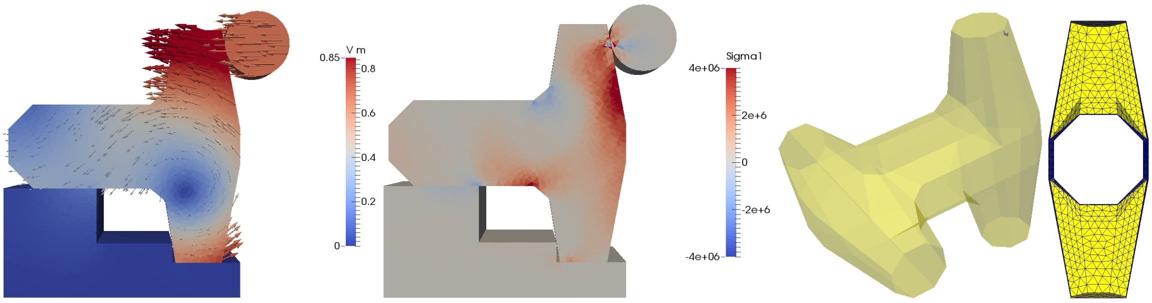

f. $t = 0.5$ ms.

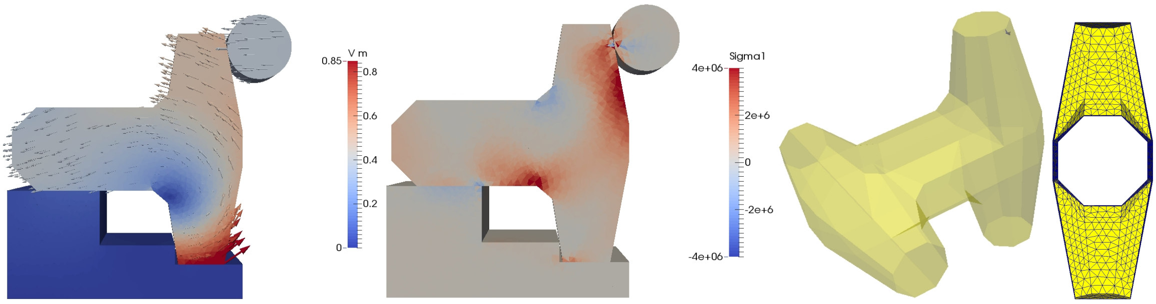

g. $t = 0.6$ ms.

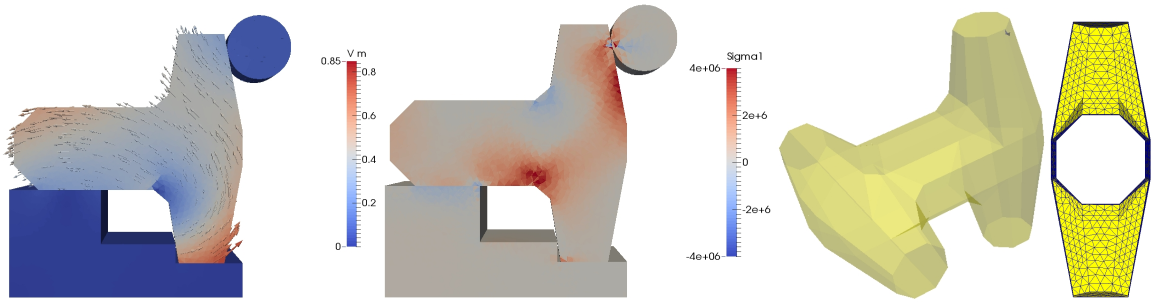

h. $t = 0.7$ ms.

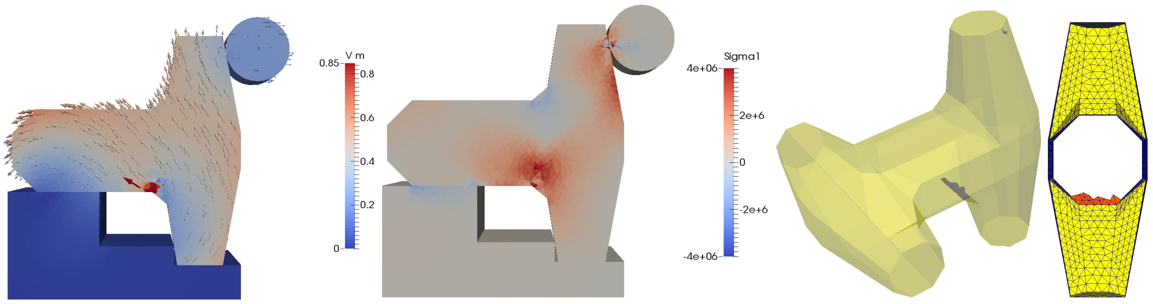

i. $t = 0.8$ ms.

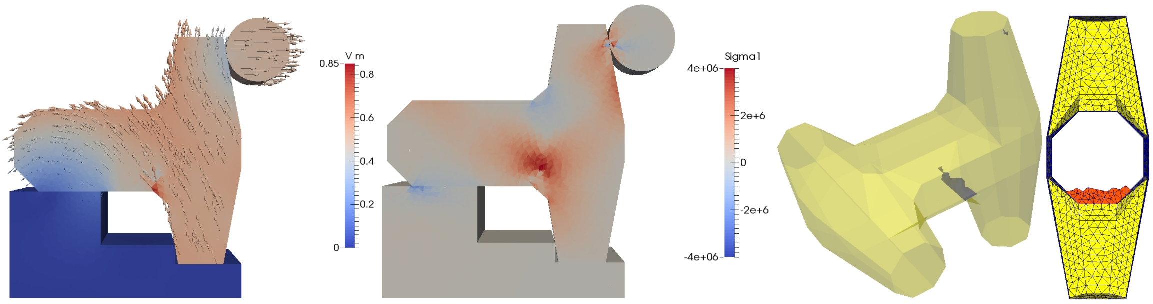

j. $t = 0.9$ ms.

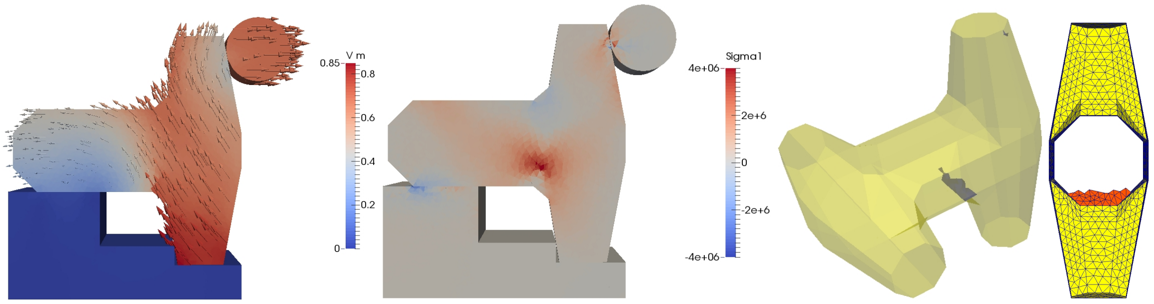

k. $t = 1.0$ ms.

Figure 17: Numerical simulation results of the pendulum test of a Dolos unit arranged in time sequence. Note that the time starts when the cylinder hits the Dolos unit. From left to right: the first column shows the velocity vector and magnitude in the cut plane perpendicular to the $z$-direction, where $v_m = \sqrt{\left(v_x^2 + v_y^2 + v_z^2\right)}$, and here the unit of velocity is m·s$^{-1}$; the second column shows the maximum principal stress $\sigma_1$ in the cut plane perpendicular to the $z$-direction, where tensile stress is positive, and compressive stress is negative, and the unit of stress is Pa; the third column shows the three-dimensional fracture development in the Dolos unit, where the semi-transparent yellow colour represents surfaces of the Dolos unit and the blue colour represents fracture surfaces; the fourth column shows the cross-section view generated by cutting the model as shown in Figure 16b, where the yellow colour represents surfaces of the Dolos unit and the orange colour represents fracture surfaces.

It can be seen that shortly after the cylinder hits the Dolos unit ($t = 0.2$ ms, Figure 17c), a very small part of the Dolos unit crushes at this impact point. This shear fracture only has the surface area of one element size and does not propagate further. Then, the stress concentration zone develops in the middle of the right boundary of the right fluke (Figure 17d and e), but the magnitude of stress here is not large enough to initiate fractures.

At $t \sim 0.8$ ms, the stress concentration in the lower stem-fluke corner is built up high enough to initiate the first tensile fracture in the Dolos unit (Figure 17i). Note that the stress concentration zone ahead of the fracture moves with the propagation of fractures from the surface to the inside; this phenomenon is accurately captured in Figure 17i-k. When the bottom end of the right fluke is detached from the base due to rotational motion caused by the strike of the cylinder, the stress field in the Dolos unit becomes relatively stable; most concentrated stresses are relieved, and only one exists at the fracture tip, but it is reducing and does not develop new fractures any more (Figure 17k). In this final fracture pattern, except the small crushing at the impact point, the fractures in the lower stem-fluke corner are the only failures in the Dolos unit.

### 3.2.3 Results of Dolosse units with pre-existing surface cracks

In the second test, several surface cracks are introduced in the upper and lower stem-fluke corners of the Dolos unit before applying impact loading (Figure 18a), which is similarly implemented as in the drop test. They extend from the surface at the chamfer connection running inside for approximately one element length (blue areas in Figure 18a).

The results of the pendulum test of the Dolos unit with pre-existing surface cracks are shown in Figure 18. It should be noted that in Figure 18 the Dolos unit is cut by two parallel planes (shown in Figure 16b) to show the fracture development inside the Dolos unit, and in the three-dimensional view of fractures a semi-transparent colour scheme is adopted. The motion and stress evolution of this Dolos unit with pre-existing surface cracks are very similar to the intact one, so only fracture development is shown here for comparison.

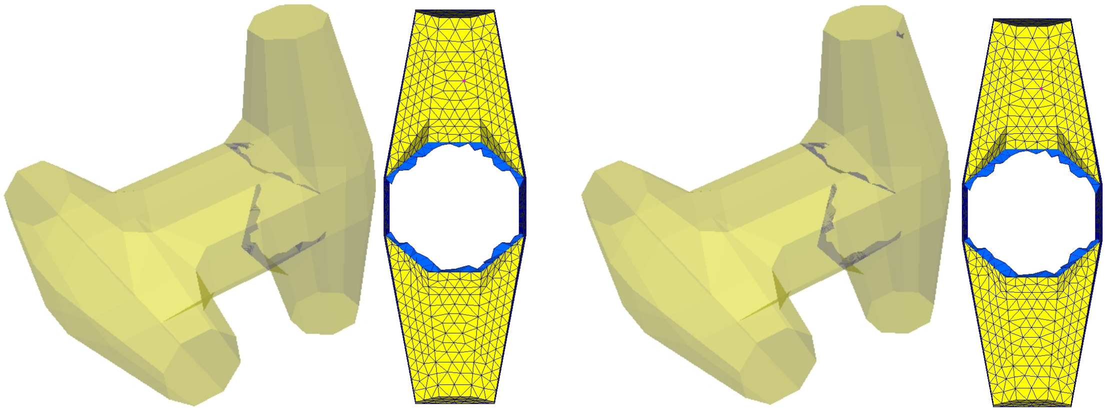

a. $t = 0$ ms.

b. $t = 0.20$ ms.

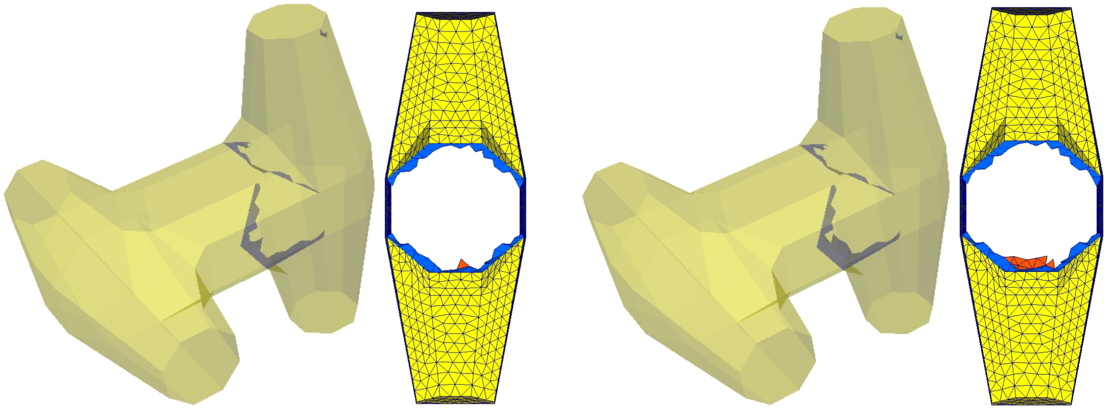

c. $t = 0.75$ ms.

d. $t = 0.80$ ms.

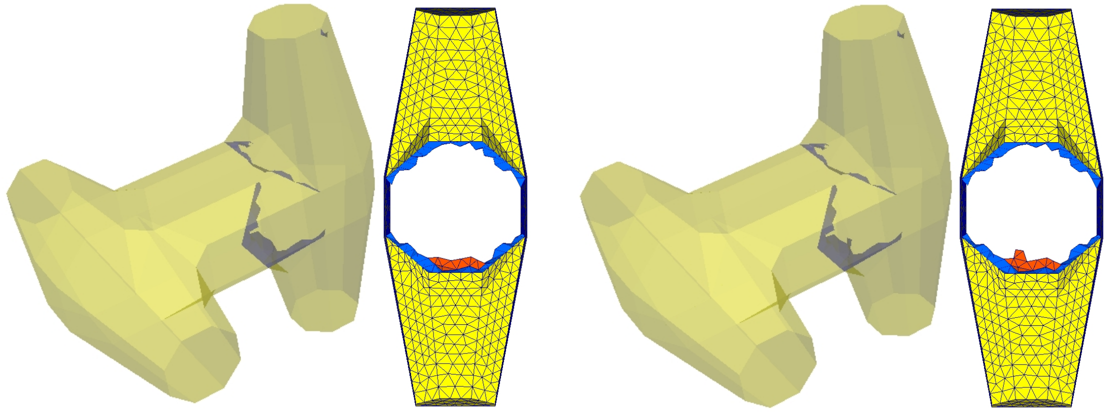

e. $t = 0.85$ ms.

f. $t = 0.90$ ms.

Figure 18: Fracture development in the pendulum test of a Dolos unit with pre-exiting surface cracks arranged in time sequence. The colour scheme used here is the same as in Figure 17.

The results of the Dolos unit with pre-existing surface cracks in the pendulum test (Figure 18) show similar fracture development as the intact units show. First, a local shear fracture of one element size develops in the right fluke at the impact point (Figure 18b). Then, new fractures propagate from the tips of pre-existing surface cracks in the lower stem-fluke corner

(Figure 18c), and extend into the Dolos unit for approximate 2-3 element lengths (Figure 18d-f). Similar to the fracture pattern formed in the intact Dolos unit, these new fractures are the only significant failures caused by the strike of the cylinder; there are no new fractures in other parts of the Dolos unit, except the local crushing at the impact point.

## 3.3 Discussion

### 3.3.1 Comparison between physical experiments and numerical simulations

One of the main objectives of this research is to validate the numerical code by comparing the numerical simulation results with Burcharth's physical experiment results (1981b). It should be noted there are two major differences between physical experiments and numerical simulations, which are listed as follows:

1. Dolosse units of full-scale dimensions were used in physical experiments (Burcharth, 1981b), which are larger than the Dolosse units tested in the numerical simulations. The simulated Dolosse units are scaled down from full-scale dimensions so that high accuracy and affordable CPU time can be guaranteed. However, this has necessitated the use of a somewhat higher drop angle for hammer drop tests and a higher swing height in the pendulum tests.
2. The Dolosse units were struck several times until they completely broke into two pieces in physical experiments (Burcharth, 1981b). Because cyclic loading and material fatigue are not taken into account in the material constitutive model applied in the FEMDEM code, the Dolosse units are only struck once in numerical simulations. Therefore, no fractures are fully developed such that they would break Dolosse units into two parts, but the locations and evolution of fractures are still accurately captured.

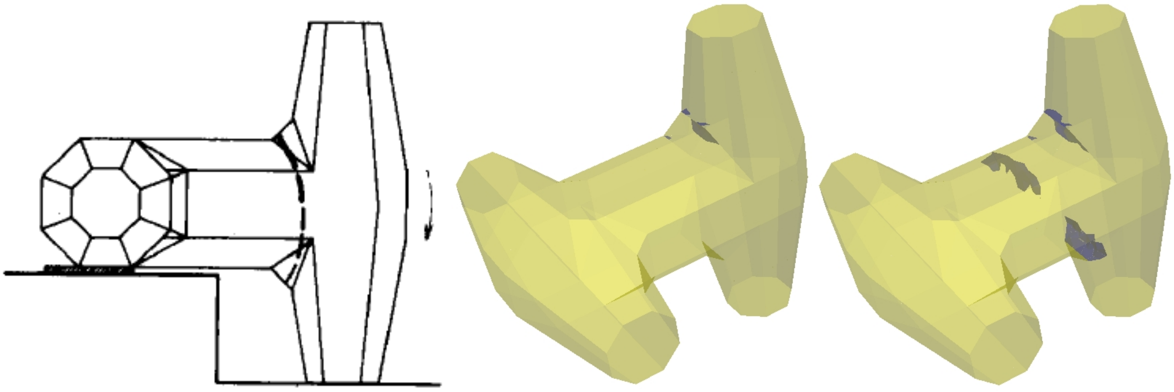

a. Physical experiment result (after Burcharth, 1981b).

b. Numerical simulation result, $t = 0.50$ ms.

c. Numerical simulation result, $t = 2.40$ ms.

Figure 19: Comparison between physical experiments and numerical simulations of drop tests of intact Dolosse units. Not that figure (a) shows the schematic summary of the observed fracture modes in Burcharth's tests (1981b).

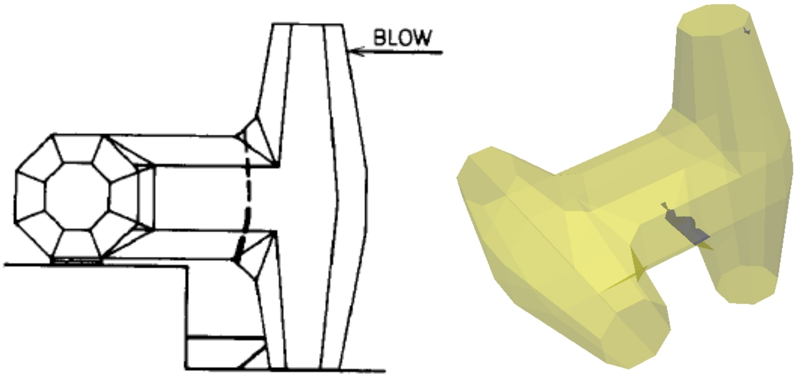

a. Physical experiment result (after Burcharth, 1981b).

b. Numerical simulation result, $t = 1.0$ ms.

Figure 20: Comparison between physical experiments and numerical simulations of pendulum tests of intact Dolosse units.

In Burcharth's results (1981b) of drop tests, it is reported that fractures initiate from the upper stem-fluke corner then spread to the lower corner (Figure 19a); it is also stated that in a few drop tests the fracturing starts through the middle part of the stem instead of the upper corner. By comparing the numerical simulation result of the drop test (Figure 19b and c) with the physical experiment result (Figure 19a), it can be seen that fractures develop in a similar way; the fracturing starts from the upper stem-fluke corner, then in the middle part of the stem, last in the lower stem-fluke corner. These fracture patterns have also been reported from real site monitoring (Myrick and Melby, 2005). Figure 21 shows typical Dolos unit breakages at Crescent City, California, USA.

a. Example of fluke-stem fracture.

b. Example of middle-stem fracture.

Figure 21: Examples of Dolos unit breakages form monitoring at Crescent City breakwater, California, USA (after Myrick and Melby, 2005).

In physical pendulum tests (Burcharth, 1981b), fractures develop in the opposite sense compared to the drop tests, and start from the lower stem-fluke corner then propagate to the upper corner (Figure 20). Similarly, in numerical simulations major fracturing develops only in the lower stem-fluke corner, and a small piece of fracture near the impact point. It is reasonable to assume that if the numerical pendulum test continues for several more strikes, the Dolos unit is most likely to break into two pieces along the path from the lower stem-fluke corner to the upper corner.

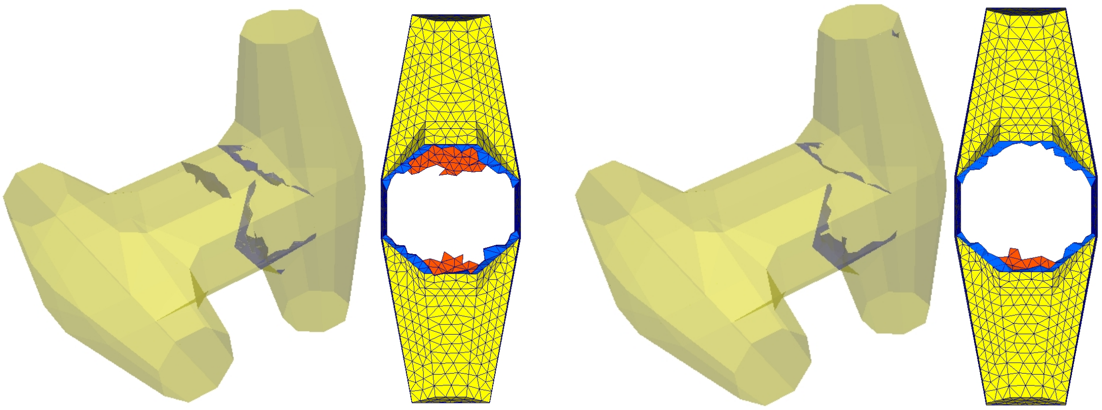

a. Drop test, $t = 2.45$ ms.

b. Pendulum test, $t = 0.90$ ms.

Figure 22: Comparison of final fracture patterns of Dolosse units with pre-existing surface cracks in the drop test and the pendulum test. The three-dimensional fractures are shown on the left-hand side of figure (a) and (b), where the semi-transparent yellow colour represents surfaces of the Dolos unit, and the blue colour represents fracture surfaces, including both pre-existing surface cracks and newly formed fractures. The cross-section view on the right-hand side is obtained by cutting the Dolos unit using two parallel planes(Figure 16b), where the yellow colour represents surfaces of the Dolos unit, and the blue colour represents pre-existing surface cracks, and the orange colour represents newly formed fracture surfaces.

The numerical simulation results of the Dolosse units with pre-existing surface cracks show similar differences between the drop test and the pendulum test as the comparison of intact Dolosse units shows. In the drop test, fractures first propagate from pre-existing surface crack tips in the upper stem-fluke corner, then in the lower corner, resulting in a larger area of new fractures in the upper corner than the lower corner (Figure 22a); in the pendulum test, major fractures only propagate from pre-existing surface crack tips in the lower stem-fluke corner without any fracturing in the upper corner (Figure 22b). These differences are consistent with the observations in physical experiments (Burcharth, 1981b).

Although the obtained fracture patterns in physical experiments and numerical simulations are representative of typical failure scenarios of Dolosse units, it is worth noting that in reality the constraints are more complex as units are always more restricted by the effects of their neighbour unit contact forces. Because stress distribution and fracture development are very sensitive to loading conditions and external constraints, the fracture patterns observed in real sites may be different from the ones obtained here.

### 3.3.2 Effect of surface cracks

a. Final fracture pattern of the intact Dolos unit in the drop test.

b. Final fracture pattern of the Dolos unit with pre-existing surface cracks in the drop test.

Figure 23: Comparison of final fracture patterns in drop tests. The semi-transparent yellow colour represents surfaces of the Dolos unit; the blue colour represents fracture surfaces, including both pre-existing surface cracks and newly formed fractures.

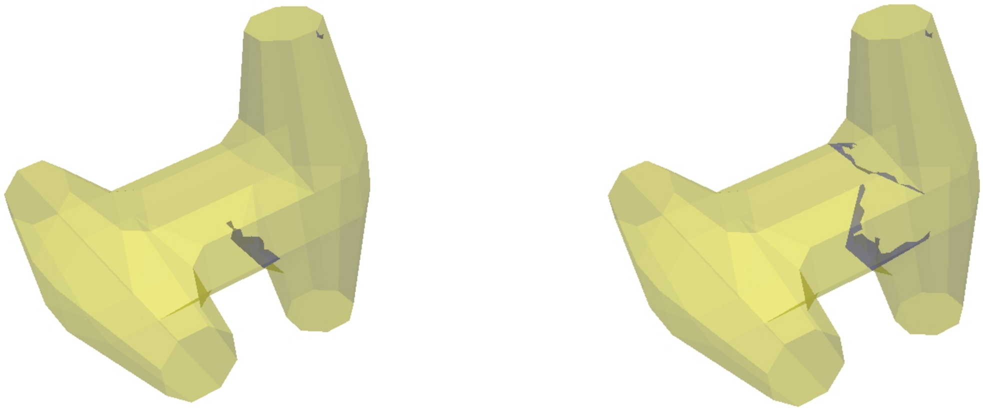

a. Final fracture pattern of the intact Dolos unit in the pendulum test.

b. Final fracture pattern of the Dolos unit with pre-existing surface cracks in the pendulum test.

Figure 24: Comparison of final fracture patterns in pendulum tests.

The effect of surface cracks on fracture development in Dolosse units subject to dynamic loading conditions are investigated by comparison between intact Dolosse units and Dolosse units with pre-existing surface cracks (Figure 23 and Figure 24). It can be seen that the main effect of the inserted surface cracks is to restrict the newly formed fractures to develop from pre-existing surface crack tips. In drop tests, fractures in the upper stem-fluke corner of the intact Dolos unit are mainly formed at the outer side of the chamfer, which is attached to the fluke; in contrast, fractures develop at the inner side of the chamfer, which is attached to the stem, for the Dolosse units with pre-existing surface cracks, because the surface cracks only exist at this side, and the new fractures propagate from pre-existing surface crack tips. In the pendulum tests, the intact Dolos unit has fractures that form more vertically in the lower stem-fluke corner; while the new fractures are developed more inclined towards the fluke in the lower corner of the Dolos unit with pre-existing surface cracks, because the surface cracks are not orientated vertically but more towards the fluke. Therefore, the surface cracks have a significant effect on the location and orientation of newly formed fractures, since the stresses are highly concentrated at these crack tips. It is worth noting that in reality surface cracks might exist anywhere in Dolosse units. The cases studied in this research represent the least safe situation, where surface cracks only exist in the right stem-fluke corners, because from the tests of intact Dolosse units it is known that fractures are most likely to form at these locations under the specific loading conditions applied here.

Another point worth noting is that surface cracks do not have a significant effect on the strength of Dolosse units. It can be seen from Figure 23 and Figure 24 that the patterns and degrees of fracturing are very similar between intact Dolosse units and Dolosse units with pre-existing surface cracks. The area of fractures formed in intact Dolosse units are of the same order of magnitude as the area of both pre-existing surface cracks and newly formed fractures in Dolosse units with pre-existing surface cracks, where only the surface cracks having new fractures propagated from them are taken into account. This point is consistent with Burcharth's (1981b) conclusion, which stated that surface cracks had negligible influence on the strength of unreinforced Dolosse units. Whereas surface cracks have minor effects on the strength of Dolosse units under dynamic loading conditions studied in this research, it does not indicate surface cracks can be ignored, as in reality they can affect the long-term durability of Dolosse units significantly.

# 4 Simulation of multi-body Core-Loc units under gravity

There are very few physical laboratory experiments reported in the literature which directly examine breakages of Core-Loc units. Turk and Melby (1998) investigated the dynamic response of Core-Loc units with laboratory scale (32 kg) and prototype scale (9.2 t) in drop tests and compared the results with Dolosse units, proving the prototype Core-Loc units are more robust than Dolosse units under tested conditions. This section is an attempt to investigate the potential of the three-dimensional fracture model to simulate possible breakages of Core-Loc units. It should be noted that the scenario for the boundary conditions and the results obtained from the numerical simulation as shown in this section cannot be taken to indicate potential failures that would be observed in Core-Loc units in reality. The simulation is purely designed for scientific research purpose.

## 4.1 Simulation setup

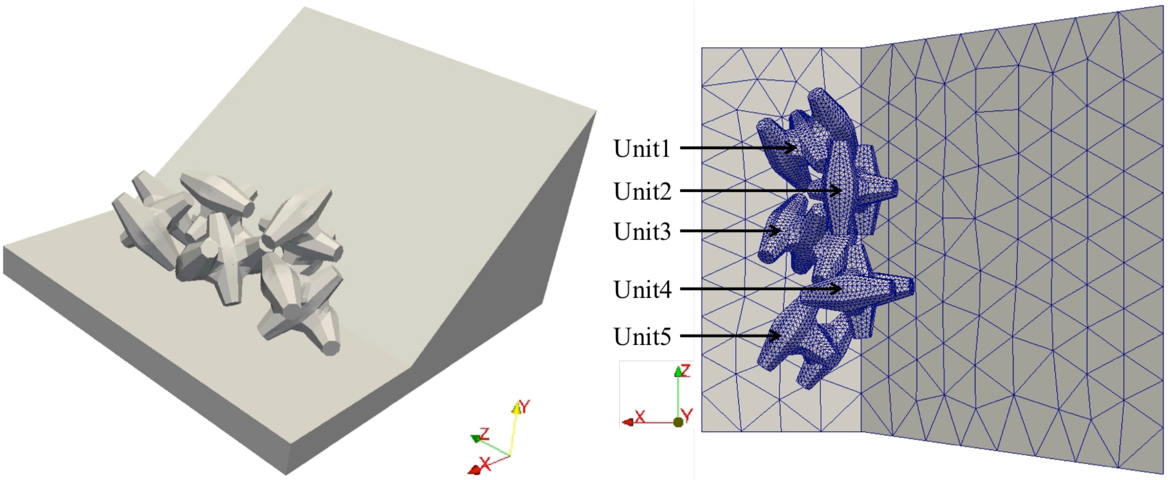

a. Model setup.

b. Mesh of the model with numerals differentiating Core-Loc uints.

Figure 25: Model setup and mesh of the simulation of multi-body Core-Loc units.

The objective of this simulation is to investigate complex multi-body interactions between Core-Loc units in an artificial situation. The system consists of five full-scale Core-Loc units (Figure 25) apparently ‘resting’ on a slope. The true boundary conditions at the beginning of the simulation are in fact that all of the five Core-Loc units are lifted a very small height

~0.016 m, and they are also positioned to be very close but not in contact with each other, with an average nearest contact distance for each unit of ~0.032 m. Therefore, when the simulation begins and they are released under gravity, they will fall down and would eventually reach a stable resting state, but during the fall process their motions will cause multiple collisions with the base slope and with each other. It should be noted that it would take a significantly longer time for the system to reach an equilibrium state of rest than the simulated time period that has been sampled here. So the final scenario ($t$ = 0.1 s) obtained from this simulation is a transient state, and does not represent any stable static situations. All of the five Core-Loc units are of the same dimensions: the length of the Core-Loc unit is 3.31 m, and the weight is 18.72 t (a volume of 8 $m^3$). The acceleration of gravity $g$ is set to be 9.8 $m/s^{-2}$.

Velocity constrained boundary conditions are applied to the base. The bottom surface of the base is restrained in the $y$-direction; the two left-hand and right-hand surfaces are restrained in the $x$-direction; and the two front and back surfaces are restrained in the $z$-direction. These conditions ensure there is no rigid body motion of the base. The fracture model is only applied to the five Core-Loc units and the viscoelastic constitutive model is applied to the base. Therefore, fracturing can only occur in the Core-Loc units, and only viscoelastic deformation without fracturing is allowed to happen in the base. In reality, however, some of the collision energy between the Core-Loc units and the base would be absorbed by local inelastic deformation at the collision point in the base, so the simulated scenarios are conservative estimations of the response of Core-Loc units as there is a maximum degree of fracturing.

The type of material assigned to the Core-Loc units and the base is unreinforced concrete. The same values are used for both the Core-Loc units and the base as in the drop tests of Dolosse units (Table 2), however the difference is the Core-Loc units are allowed to break, but the base can only viscoelastically deform without breaking. The friction coefficient $\mu$ between Core-Loc units, and between Core-Loc units and the base is set to be 0.6. A brief discussion of the selection of values of $\mu$ was given in Latham et al. (2013).

The whole domain is meshed by unstructured 4-node tetrahedral elements (Figure 25b). The same mesh size is assigned to all five Core-Loc units, which is approximately 0.15 m. The base uses a coarser mesh, with average element size of 1.5 m. A total number of 98734 tetrahedral elements are generated. Each Core-Loc unit consists of 19331 elements, and the base consists of 2079 elements. A time-step $\Delta t = 2 \times 10^{-7}$ s is used in the numerical simulation. A point to note is that in this simulation, Core-Loc units of full-scale dimensions are simulated, so the element size is much larger than the element size used for Dolosse units of ~1 m. This is due to the consideration of achieving affordable CPU time and guaranteeing the accuracy is still acceptable.

## 4.2 Results

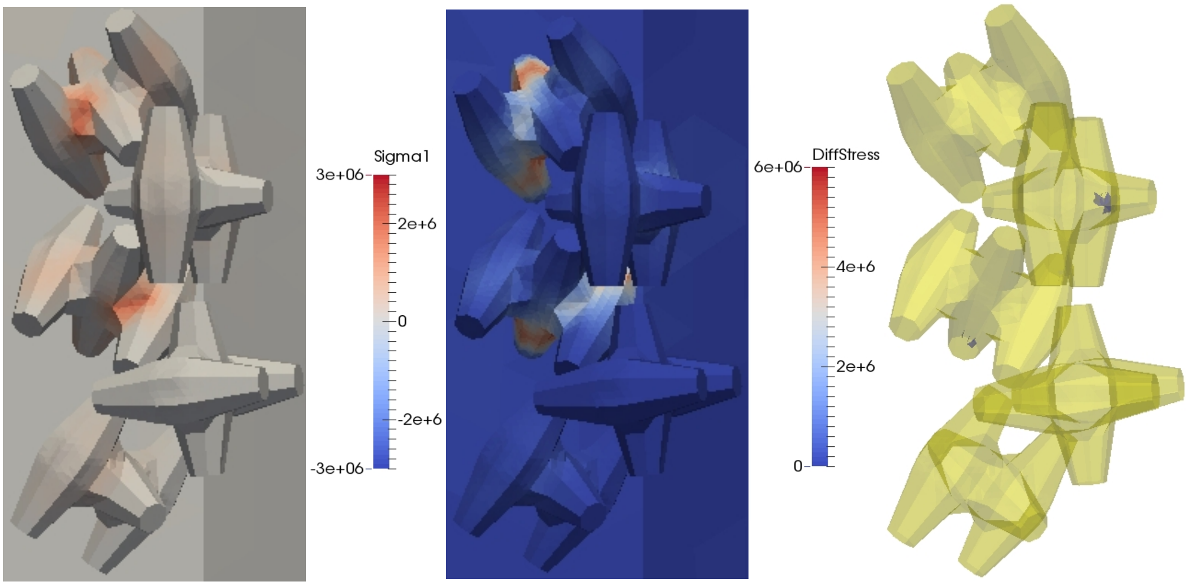

a. $t = 0.061$ s.

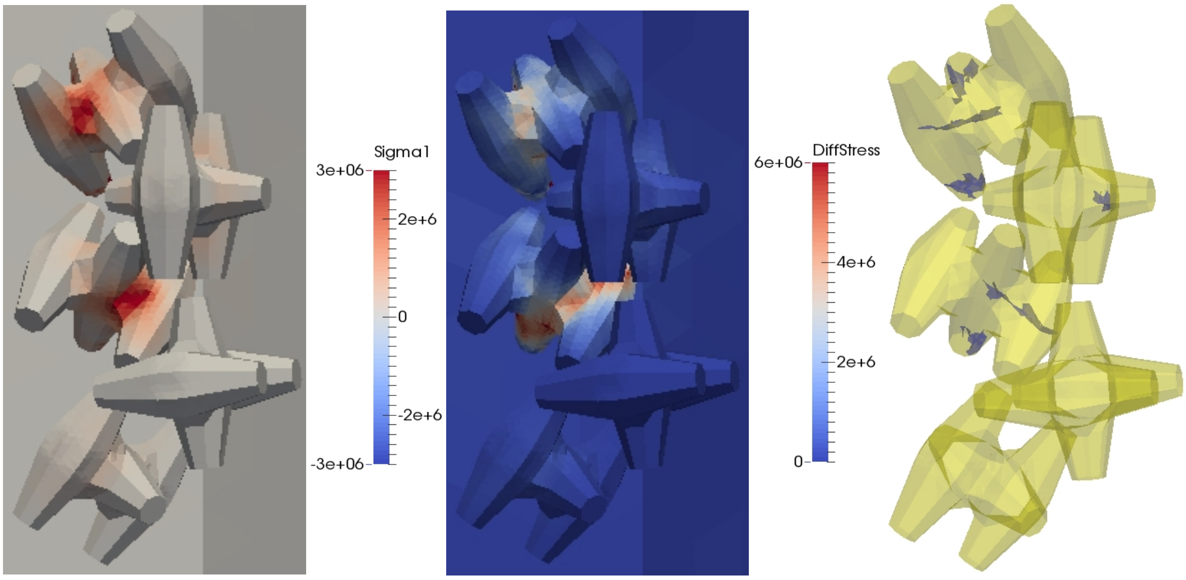

b. *t* = 0.063 s.

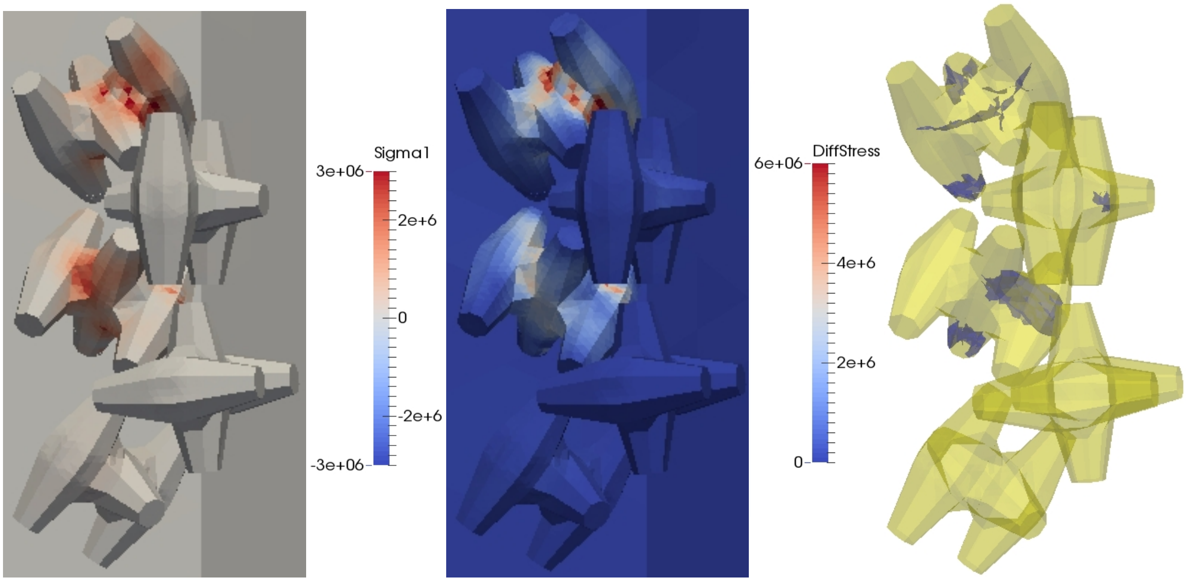

c. *t* = 0.067 s.

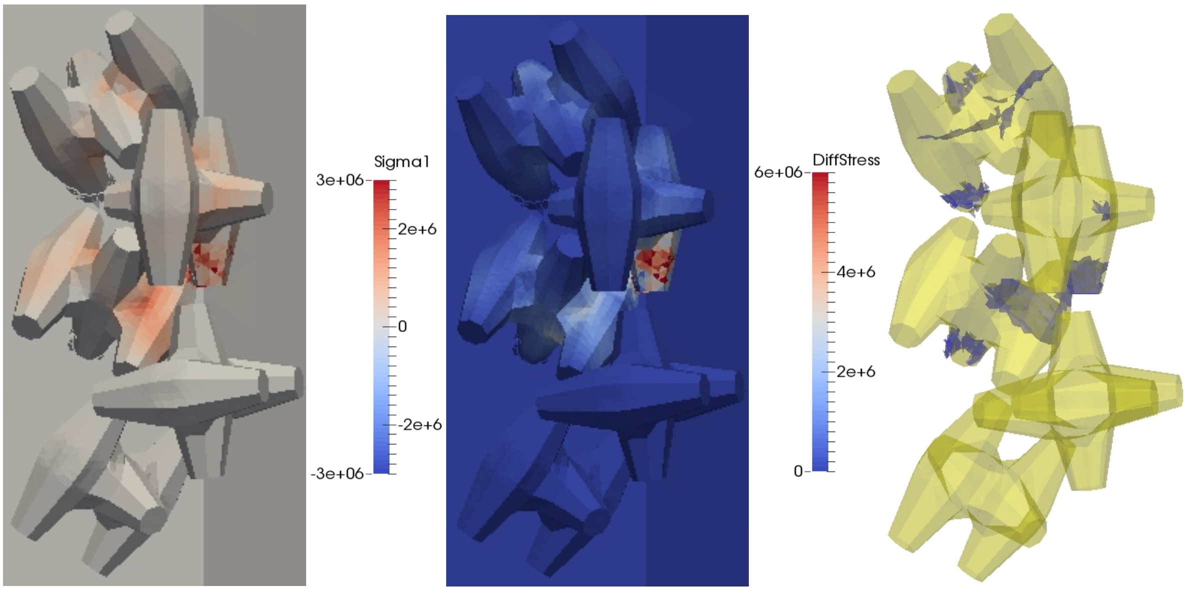

d. $t = 0.084$ s.

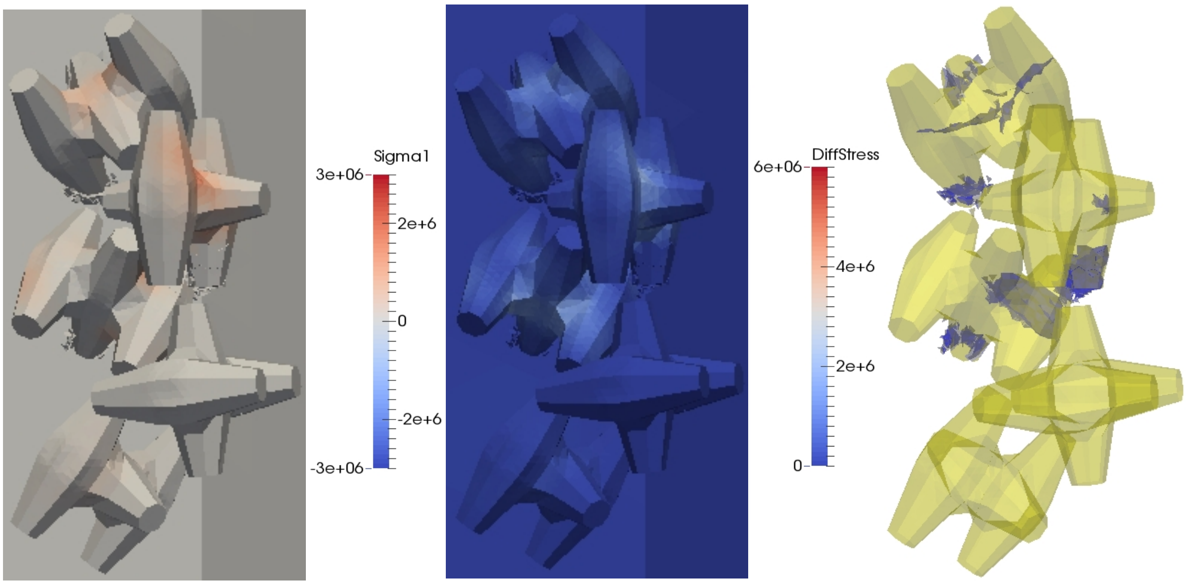

e. $t = 0.100$ s.

Figure 26: Numerical simulation results of interaction between multi-body Core-Loc units under gravity on a slope base. The left-hand column shows maximum principal stress $\sigma_1$, where tensile stress is positive, and compressive stress is negative. The middle column shows differential stress $\sigma_D = \sigma_1 - \sigma_3$. The right-hand column shows three-dimensional fractures using a semi-transparent colour scheme, where the yellow colour represents surfaces of Core-Loc units, and the blue colour represents fracture surfaces.

The simulation models a period of real time of 0.1 s. The evolution of stresses and fractures are shown in Figure 26. Because of the complex geometry of Core-Loc units, even under relatively simple loading conditions, which is only gravity, the stress field in the system is very complicated. Therefore, it is hard to say fractures are caused purely by tensile failures or shear failures. By comparing the three figures in each row of Figure 26, it can be seen that most fractures are caused by a combination of effects including both excessive tensile stresses and differential stresses.

## 4.3 Discussion

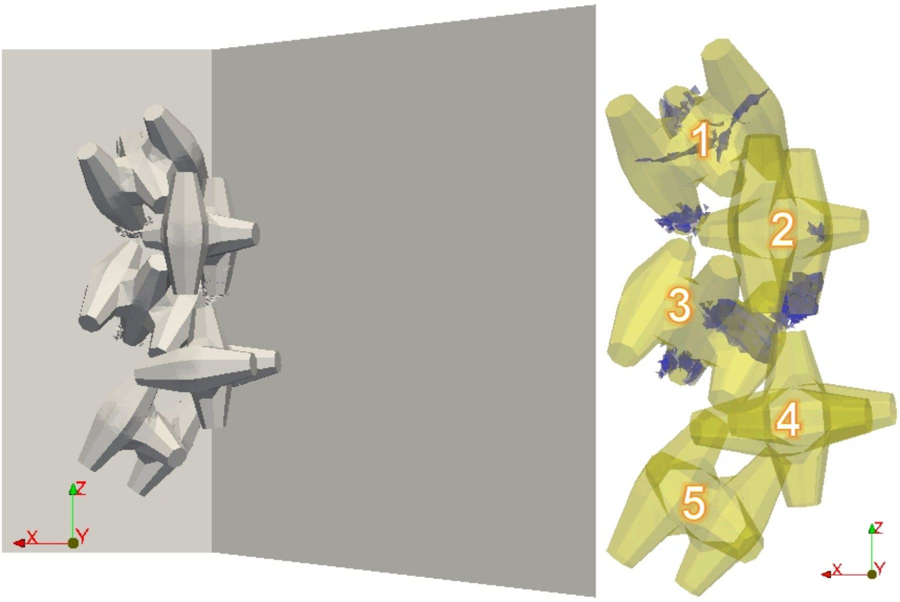

Figure 27: Transient failure scenario of Core-Loc units at time *t* = 0.1 s. On the left-hand side, a global figure shows the transient state of these five Core-Loc units after 0.1 s under gravity. On the right-hand side, a semi-transparent colour scheme is used to show fracture development inside the Core-Loc units. The yellow colour represents surfaces of Core-Loc units, and the blue colour represents fracture surfaces. See numerals to differentiate Core-Loc units.

The transient state of the five Core-Loc units at *t* = 0.1 s is shown in Figure 27. The results of this simulation are further analysed by plotting the energy in the system versus time. It is known that fracturing behaviour cause energy dissipation, so by analysing the energy evolution in the system, fracturing events can be identified by a corresponding energy loss. This is based on the assumption that fracturing behaviour is the only or dominant energy dissipation mechanism in the system, which is valid in this simulation. In the numerical code, energy can be dissipated by three mechanisms: viscous damping, friction, and fracturing. The first two mechanisms in the fracturing simulation work in the same way as in the purely elastic simulation. Only the fracture model introduces the third mechanism into the system to dissipate energy. Therefore, by comparing results of the fracturing simulation and the elastic simulation, the energy dissipated by fracturing can be clearly identified.

Here two forms of energy are calculated: gravitational potential energy $E_p$ (Equation 6) and kinetic energy $E_k$ (Equation 7),

$$E_p = \sum_{i=1}^{N} m_i g h_i \tag{15}$$

$$E_k = \frac{1}{2}\sum_{i=1}^{N} m_i v_i^2 \tag{16}$$

where $E_p$ is the total gravitational potential energy of each Core-Loc unit, $E_k$ is the total kinetic energy of each Core-Loc unit, $N$ is the total number of element nodes on the numerical mesh associated with each Core-Loc unit, $m_i$ is the mass of node $i$ on the mesh, $h_i$ is the vertical distance between node $i$ and the surface of zero gravitational potential energy, which is assumed to be the upper horizontal surface of the base, $v_i$ is the velocity magnitude of node $i$.

### 4.3.1 Unbroken and non-colliding unit (unit 4)

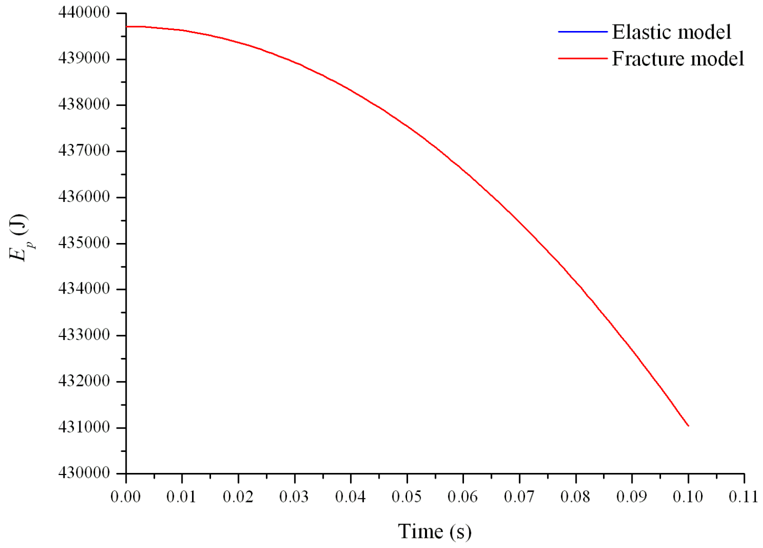

a. Gravitational potential energy $E_p$.

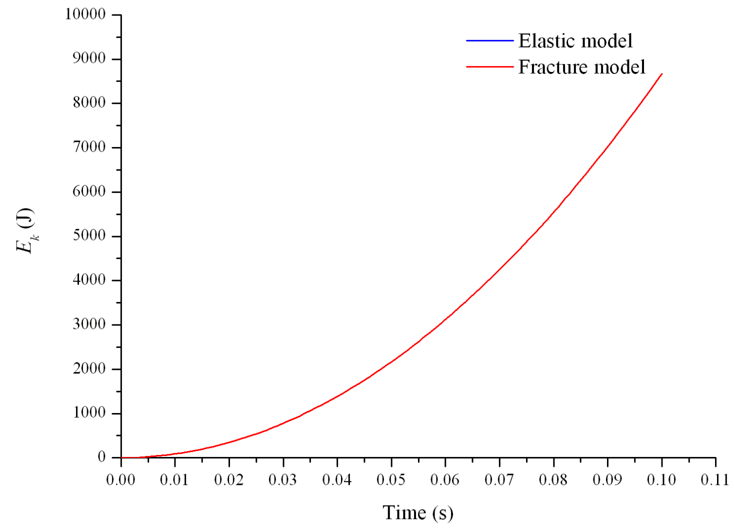

b. Kinetic energy $E_k$.

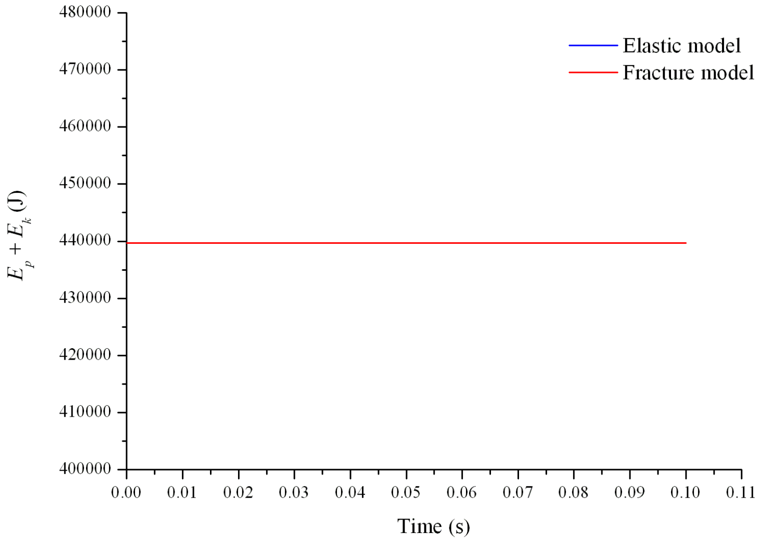

c. Energy $E_p + E_k$.

Figure 28: Time histories of energy of Core-Loc unit 4. Graph (a), (b) and (c) show plots of gravitational potential energy $E_p$, kinetic energy $E_k$, and energy sum $E_p + E_k$ of Core-Loc unit 4 versus time, respectively. The red line is the simulation result using the fracture model, and the blue line is the result using the viscoelastic model. Note that the blue line cannot be seen because it is masked by the red line.

From Figure 27 it can be seen that Core-Loc unit 4 does not break. Through careful checking of its motion during the simulation, it is found that it also does not collide with the base or the other Core-Loc units. Thus, during the simulation time, the motion of Core-Loc unit 4 is purely free falling. This can be clearly validated in the energy plots shown in Figure 28. Because there is no form of energy dissipation in Core-Loc unit 4, the curves from the fracturing simulation complete overlap the curves from the elastic simulation. Therefore, the blue line cannot be seen because it is masked by the red line. It should also be noted that in the numerical simulation, energy is perfectly conserved (Figure 28c).

### 4.3.2 Unbroken but colliding unit (unit 5)

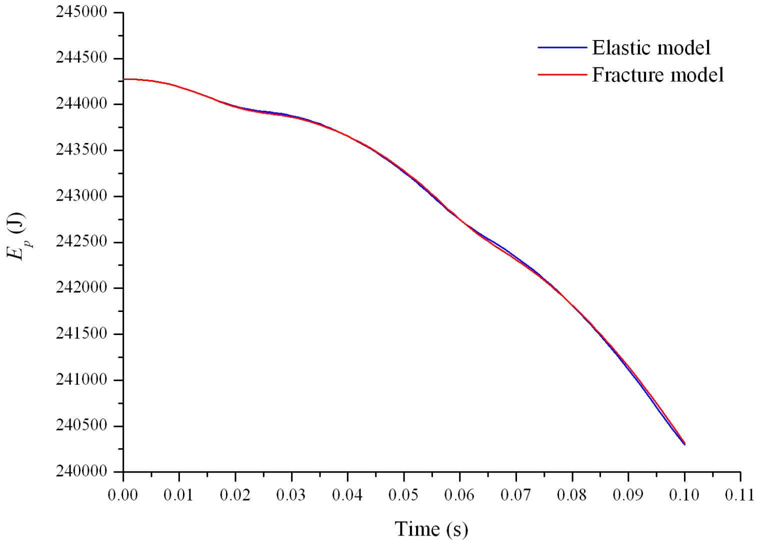

a. Gravitational potential energy $E_p$.

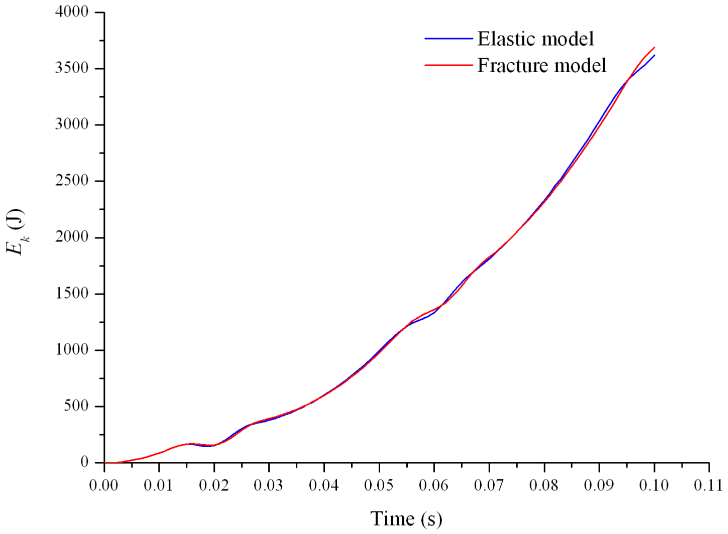

b. Kinetic energy $E_k$.

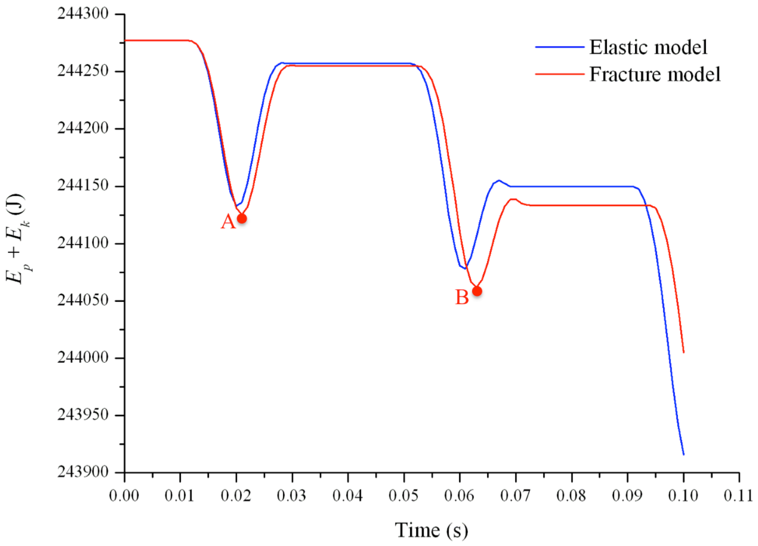

c. Energy $E_p + E_k$.

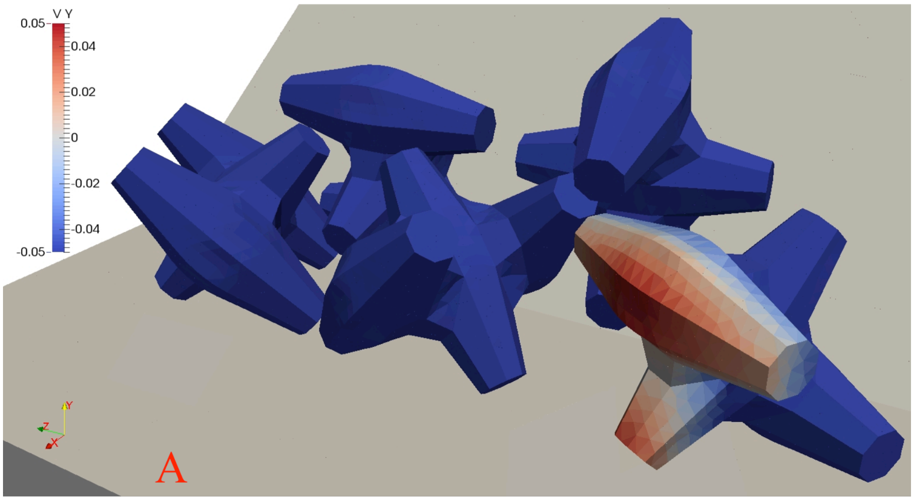

d. Vertical velocity contour at $t$ = 0.021 s.

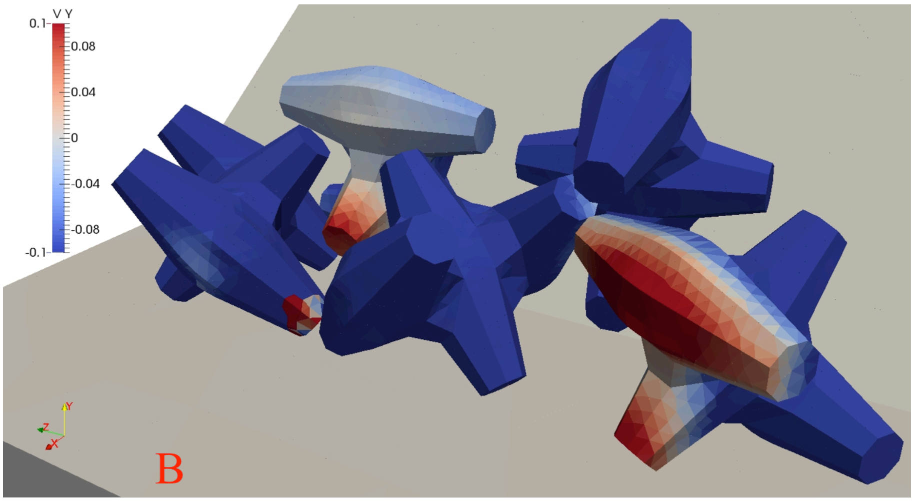

e. Vertical velocity contour at $t$ = 0.063 s. Note that the magnitude of velocity in this figure is greater than figure (d).

Figure 29: Time histories of energy of Core-Loc unit 5. Figure (d) and (e) show vertical velocity contours (*y*-direction) at two specific moments $t = 0.021$ s and $t = 0.063$ s, corresponding to point A and point B in graph (c) respectively.

Core-Loc unit 5 does not break but collides with the base during the simulation period. The energy loss caused by the collision events can be identified especially in Figure 29c. There are two energy drops in Figure 29c; each corresponds to one collision event (Figure 29d and Figure 29e). By comparing the velocity magnitude of Core-Loc unit 5 (the right-most one) in Figure 29d and Figure 29e, it can be seen that the second collision (Figure 29e) is more severe than the first one (Figure 29d), which generate vertical colliding velocities of ~0.1 $\mathrm{m \cdot s^{-1}}$ and ~0.05 $\mathrm{m \cdot s^{-1}}$ to Core-Loc unit 5, respectively. The viscous damping is relevant to velocity gradient, so the second collision dissipates more energy than the first one, resulting in a greater drop on the energy plot (Figure 29c).

There are two points to note here. First, the energy is only calculated in the form of gravitational potential energy $E_p$ and kinetic energy $E_k$. The indentations on the plot of energy sum $E_p + E_k$ mean the energy is being transformed into elastic deformational energy in Core-Loc unit 5 during the collisions. The elastic strain energy is recovered once Core-Loc unit 5 bounces off the base. Second, there is a small gap between the curves from the fracturing simulation and the ones from the elastic simulation, especially in Figure 29c. This is due to the difference in stiffness caused by introducing joint elements for the fracture model. The system becomes more compliant after adding joint elements, which causes a small delay in the response of the system.

### 4.3.3 Broken units (units 1, 2 and 3)

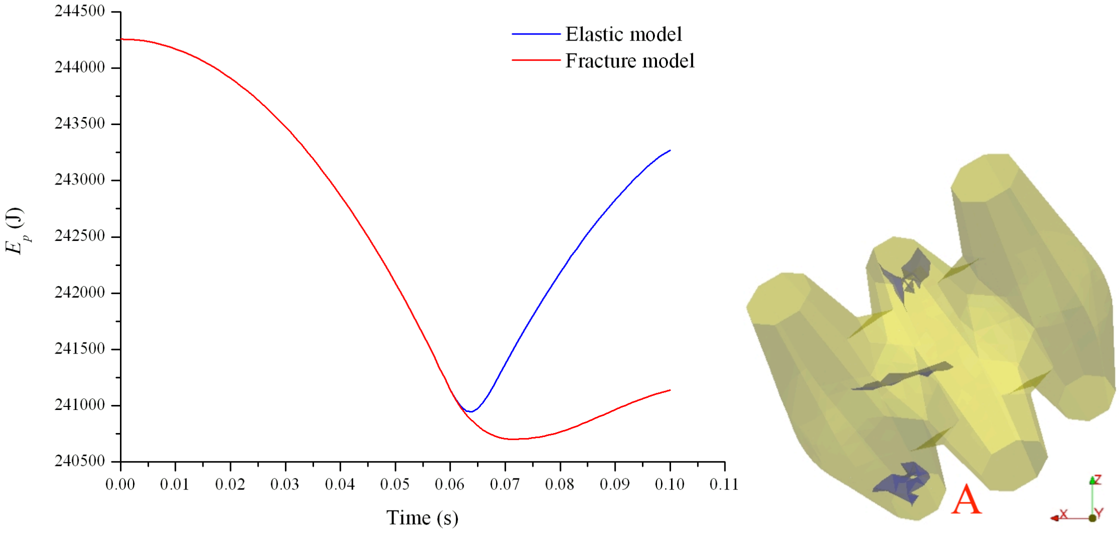

a. Gravitational potential energy $E_p$.

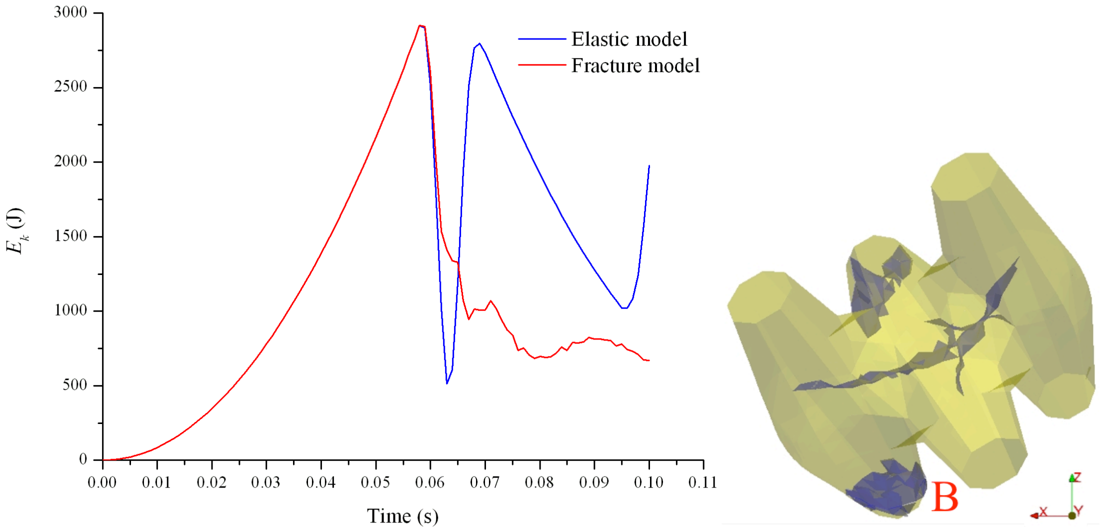

b. Kinetic energy $E_k$.

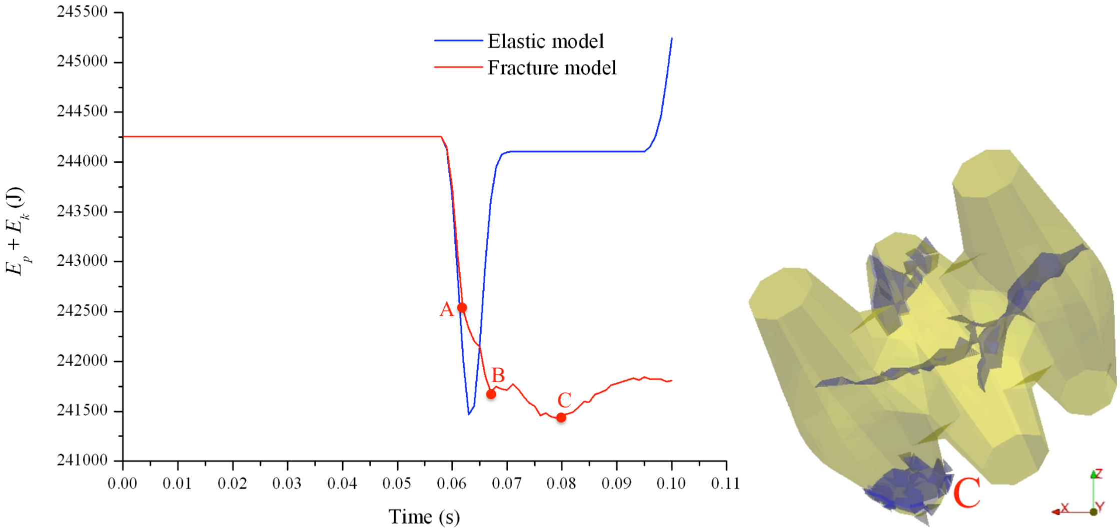

c. Energy $E_p + E_k$.

Figure 30: Time histories of energy of Core-Loc unit 1. On the left-hand side, graph (a), (b) and (c) show plots of gravitational potential energy $E_p$, kinetic energy $E_k$, and energy sum $E_p + E_k$ of Core-Loc unit 1 versus time, respectively. The red line is the simulation result using the fracture model, and the blue line is the result using the viscoelastic model. On the right-hand side, three figures show three-dimensional fractures at three specific moments corresponding to point A ($t$ = 0.062 s), point B ($t$ = 0.067 s) and point C ($t$ = 0.080 s) in graph (c), respectively.

Core-Loc units 1, 2 and 3 break during the simulation period (Figure 27). Here unit 1 is taken as an example and the energy evolution is plotted in Figure 30. It can be seen that fracturing events are always accompanied by energy losses. This can be validated by comparing plots of energy sum $E_p + E_k$ from the fracturing simulation and the elastic simulation (Figure 30c). It can also be seen that all fractures are initiated by collisions. In the elastic simulation, the energy can be mostly or entirely restored after collisions. In the fracturing simulation, however, because collisions always cause fracturing, energy cannot be restored but is dissipated during collisions.

### 4.3.4 Diversity of failure modes

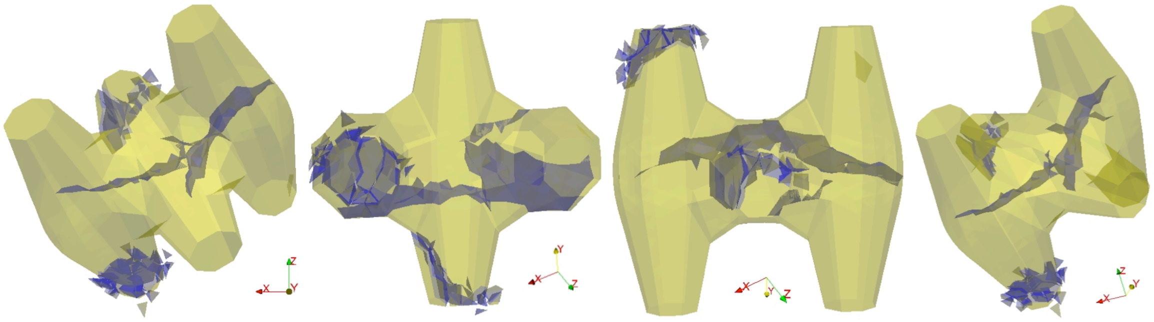

a. b. c. d.

Figure 31: Three-dimensional view of transient failure pattern of Core-Loc unit 1 at $t$ = 0.1 s from different angles. The first one from the left is the original orientation as shown in Figure 27. Note that the semi-transparent yellow colour represents surfaces of the Core-Loc unit, and the blue colour represents fracture surfaces.

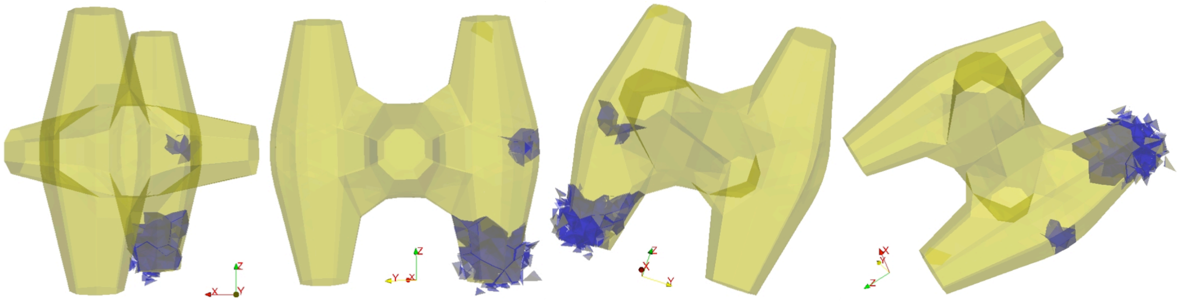

a. b. c. d.

Figure 32: Three-dimensional view of transient failure pattern of Core-Loc unit 2 at $t = 0.1$ s from different angles. The first one from the left is the original orientation as shown in Figure 27.

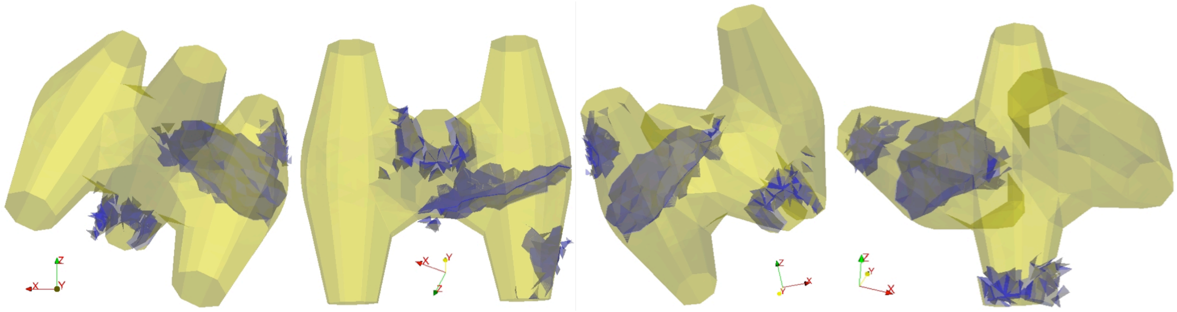

a. b. c. d.

Figure 33: Three-dimensional view of transient failure pattern of Core-Loc unit 3 at $t = 0.1$ s from different angles. The first one from the left is the original orientation as shown in Figure 27.

Different failure modes are generated by the complex stress field in this simulation. Transient failure modes of Core-Loc units 1, 2 and 3 at the end of the simulation are shown in Figure 31, Figure 32, and Figure 33, respectively. For each figure, the fractures are viewed from four different angles to fully exhibit the three-dimensional situations. Straight and clean fractures of large areas are formed in Core-Loc unit 1 (Figure 31) and Core-Loc unit 3 (Figure 33). Especially in Core-Loc unit 3 (Figure 33), a major fracture develops in the middle of unit, which would cut it into two pieces and cause fatal failure with respect to structural integrity. Crushing usually happens at the ends of Core-Loc units where they collide with the base or the other units. Crushing generates many small pieces and fragments down to element size, but this behaviour is very localised to small areas near the impact points. It is worth mentioning that the crushing behaviour can be simulated more realistically if finer mesh is employed, but that will need much longer CPU time. Typical shear failure can also be seen particularly in Core-Loc unit 1 (Figure 31c), where a shear fracture cuts off the top end of the unit.

The simulations of Dolosse units and Core-Loc units show that the three-dimensional fracture model within the FEMDEM method is capable of capturing the whole process of fracturing in complex stress fields. However, the current code still has some limitations, which set out the directions for future work. One major challenge is to realistically represent the extreme wave loading of a design storm in the model. At present, the code cannot simulate cyclic rocking of armour units because cyclic loading and material fatigue are not taken into account in the material constitutive model applied in the FEMDEM code. Once the material constitutive model has been improved in this aspect, the wave actions can be applied in two possible ways. The first one is to apply a wave proxy, which simplifies wave impacts as cyclic loading conditions (Xiang et al., 2013). In the wave proxy, drag forces and buoyancy forces are applied to the armour units to represent the effects of wave run-up and run-down and periodic submergence. The second one is to couple the FEMDEM method with a CFD (Computational Fluid Dynamics) code, e.g. Fluidity (Viré et al., 2012), and set up models with both solids domain (armour units, slope base, etc.) and fluids domain (wave action, etc.), so the wave loading on structures can be realistically simulated.

Another major challenge to the numerical modelling of such coastal structures is to significantly boost the simulation speed. The current algorithms of the fracture model and contact mechanics are complicated, resulting in unaffordable CPU time for large-scale problems. However, to fully understand the structural behaviour of prototype armour units and correctly represent the complex constraints received from surrounding units, not only should the dimensions of armour units be those of full-scale but also the number of armour units considered should be sufficient to represent the stochastic variability of a real section of breakwater trunk. This demands a significant increase in computational time and resources. In this respect, mesh adaptivity and code parallelisation are believed to offer the best strategy for a solution.

# 5 Conclusions

The new three-dimensional fracture model in the context of the FEMDEM method was applied to the investigation of the structural integrity of concrete armour units under dynamic and extreme loading conditions. Dolosse units were simulated in drop tests and pendulum tests, and the numerical results were compared with physical experiments and observations from site. Core-Loc units of prototype scale were simulated under an imaginary extreme loading condition, which represented a close but not touching configuration of interlocking units that were lifted, then dropped from slightly above a horizontal and sloping base. The results of Core-Loc units were thoroughly analysed from an energy point of view.

The whole structural response of concrete armour units, which includes multi-body interaction, rigid-body motion, continuum deformation, fracture initiation and propagation, and post-fracturing interaction between discrete fracture surfaces, was accurately captured by three-dimensional numerical simulations. Transient dynamic response including that by fracturing was explicitly characterised. Various failure modes in complex stress fields were obtained. The energy-based analysis provides a helpful tool to identify the degree of fracturing in the system, which is an important factor for the mechanical stability and long-term structural integrity assessment of the breakwater. The results give an insight into the understanding of progressive damage and reserve stability of a system of essentially strong but breakable concrete units. Provided that the loading of waves can be realistically applied and that the CPU power and run time become available, the potential of the new fracture model in the FEMDEM program has been demonstrated. A step has been taken on the journey towards providing a numerical technology for consideration of different concrete armour unit types and armour layer designs with respect to frequency and mode of failure in response to wave actions.

# Acknowledgements

This paper is part of the PhD project of the first author: *Development of a three-dimensional fracture model for the combined finite-discrete element method*. We are grateful for the support from Janet Watson scholarship provided by the Department of Earth Science and Engineering, Imperial College London for this PhD project.

## References

Appleton, W. S., Kendall, T., and Melby, J. A. (1996). A ten-year history of Dolos monitoring at Crescent City. In *Proceedings of the 25th International Conference on Coastal Engineering*, 4664-4675, Reston, USA.

Burcharth, H. F. (1981a). A design method for impact-loaded slender armour units. In ASCE *International Convention*, New York, USA.

Burcharth, H. F. (1981b). Full-scale dynamic testing of Dolosse to destruction. *Coastal Engineering*, 4:229-251.

Burcharth, H. F. (1983). Material, structural design of armour units. In *Seminar on Rubble Mound Breakwaters*, Stockholm, Sweden.

Burcharth, H. F. (1987). The lessons from recent breakwater failures, developments in breakwater design. In *World Federation of Engineering Organizations Technical Congress*, Vancouver, Canada.

Burcharth, H. F., Howell, G. L., and Liu, Z. (1991). On the determination of concrete armour unit stresses including specific results related to Dolosse. *Coastal Engineering*, 15:107-165.

Burcharth, H. F., Liu, Z., Howell, G. L., and McDougal, W. G. (1990). Stresses in Dolosse. In *Proceedings of the 22nd International Conference on Coastal Engineering*, 1417-1430, Delft, Netherlands.

CIRIA, CUR, CETMEF. (2007). *The Rock Manual. The use of rock in hydraulic engineering*. C683. London: CIRIA, second edition.

Franco, L., Noli, A., De Girolamo, P. and Ercolani, M. (2000). Concrete strength and durability of prototype tetrapods and dolosse: results of field and laboratory tests. *Coastal Engineering*, 40:207-219.

Hall, R. L., Bevins, T. L., and Howell, G. L. (1987). Drop tests of dolos armor units. In *Proceedings of the 1987 ASCE Structures Congress, Dynamics of Structures*.

Howell, G. L. (1988). Measurements of forces on Dolos armor units at prototype scale. In *Proceedings of the 21st International Conference on Coastal Engineering*, 2355-2369, Torremolinos, Spain.

Kendall, T. R. and Melby, J. A. (1992). Movement and static stress in Dolosse: six years of field monitoring at Crescent City. In *Proceedings of the 23rd International Conference on Coastal Engineering*, 1285-1298, Venice, Italy.

Kolsky, H. (1964). Stress waves in solids. *Journal of sound and vibration*, 1(1): 88-110.

Latham, J.-P., Anastasaki, E. and Xiang, J. (2013). New modelling and analysis methods for concrete armour unit systems using FEMDEM. *Coastal Engineering*, 77:151-166.

Lin, W. M., Rau, C., and Su, R. L. (1986). The structural responses of Dolos armor units under the dynamic loading. In *Proceedings of the 20th International Conference on Coastal Engineering*, 2065-2078, Taipei, Taiwan.

Melby, J. A. (2002). Kaumalapau, Hawaii, Breakwater Core-Loc strength investigation. *Report from Coastal and Hydraulics Laboratory, US Army Engineer Research and Development Center.*

Munjiza, A. (2004). *The combined finite-discrete element method.* New York: Wiley and Sons, first edition.

Munjiza, A., Andrews, K. R., and White, J. K. (1999). Combined single and smeared crack model in combined finite-discrete element analysis. *International Journal for Numerical Methods in Engineering*, 44:41-57.

Myrick, G. B. and Melby, J. A. (2005). Monitoring of Dolos armor units at Crescent City, California. *Coastal and Hydraulics Laboratory, U.S. Army Engineering Research and Development Center*, Final Report ERDC/CHL TR-05-10.

Rosson, B. T. and Tedesco, J. W. (1992). Dynamic response of Dolos armor units to drop test impact loads. *Ocean Engineering*, 19(6): 573-599.

Rosson, B. T. and Tedesco, J. W. (1993). Dynamic response of Dolos armor units to pendulum impact loads. *Computers & Structures*, 47(4/5):641-652.

Scott, D., Turcke, D., and Baird, W. F. (1990). Structural modeling of Dolos armor units. *Journal of Waterway, Port, Coastal, and Ocean Engineering*, 116:120-136.

Tedesco, J. W., McDougal, W. G., Melby, J. A., and McGill, Preston. (1987). Dynamic response of Dolos armor units. *Computers & Structures*, 26(1/2):67-77.

Tedesco, J. W., Rosson, B. T., and McDougal W. G. (1991). Numerical simulation of Dolos drop tests. *Computers & Structures*, 40(2):243-255.

Tedesco, J. W., Rosson, B. T., and Melby, J. A. (1992). Static stresses in Dolos concrete armor units. *Computers & Structures*, 45(4):733-743.

Terao, T., Terauchi, K., Ushida, S., Shiraishi, N., Kobayashi, K., and Gahara, H. (1982). Prototype testing of Dolosse to destruction. In *Proceedings of the 18th International Conference on Coastal Engineering*, 2062-2078, Cape Town, South Africa.

Timco, G. W. (1984). On the stability criterion for fracture in Dolos-armoured breakwaters. *Coastal Engineering*, 8:161-170.

Tsuji, Y., Kawaguchi, T, and Tanaka, T. (1993). Discrete particle simulation of two-dimensional fluidized bed. *Powder Technology*, 77:79-87.

Turk, G. A. and Melby, J. A. (1998). Impact structural response of Core-Loc. In *Proceedings of the 26th International Conference on Coastal Engineering*, 1846-1856, Copenhagen, Denmark.

Viré, A., Xiang, J., Milthaler, F., Farrell, P. E., Piggott, M. D., Latham, J.-P., … Pain, C. C. (2012). Modelling of fluid–solid interactions using an adaptive mesh fluid model coupled with a combined finite–discrete element model. *Ocean Dynamics*, 62:1487-1501.

Xian, L., Bicanic, N., Owen, D. R. J., and Munjiza, A. (1991). Rock blasting simulation by rigid body dynamics analysis and rigid brittle fracturing model. In Bicanic et al., editors, *Proceedings NEC-91, International Conference on Nonlinear Engineering Computations*, 577-587, Pineridge Press, Swansea, UK.

Xiang, J., Munjiza, A., and Latham, J.-P. (2009). Finite strain, finite rotation quadratic tetrahedral element for the combined finite–discrete element method. *International Journal for Numerical Methods in Engineering*, 79: 946-978.

Xiang, J., Latham, J.-P., Viré, A., Anastasaki, E., and Pain, C. C. (2013). Numerical modelling of wave – rubble mound breakwater interaction. In *Proceedings of the 6th International Conference on Discrete Element Methods (DEM6)*, 426-431, Golden, USA.

Zwamborn, J. A. and Scholtz, J. D. P. (1986). Dolos armor design considerations. In *Proceedings of the 20th International Conference on Coastal Engineering*, 2420-2434, Taipei, Taiwan.

Zwamborn, J. A. and Scholtz, J. D. P. (1988). Stability and structural behaviour of strength improved dolosse. In *Proceedings of the 21st International Conference on Coastal Engineering*, 2075-2089, Malaga, Spain.